Freie Universität Berlin

Application and Cellular Interaction of Cationic Nanoparticles

Dissertation

zur Erlangung des akademischen Grades des

Doktors der Naturwissenschaften (Dr. rer. nat.)

eingereicht im Fachbereich Biologie, Chemie, Pharmazie der

Freien Universität Berlin

Vorgelegt von

Falko Neumann, M. Sc.

aus Berlin

Dezember 2017

Diese Arbeit wurde unter der Anleitung von Prof. Dr. Nan Ma und Prof. Dr. Rainer Haag im Zeitraum von Mai 2014 bis Dezember 2017 am Institut für Chemie und Biochemie der Freien Universität Berlin angefertigt.

1. Gutachter	Prof. Dr. Nan Ma
2. Gutachter	Prof. Dr. Rainer Haag
vorgelegt von	Falko Neumann
Disputation am	11.04.2018

Acknowledgement

First and foremost, I would like to thank Prof. Dr. Nan Ma and Prof. Dr. Rainer Haag for the chance to do my PhD thesis in close cooperation of and with the support of two groups.

Furthermore, I would like to thank the members of both the Ma and Haag groups for a nice lab atmosphere and fruitful discussions.

Thanks go to the people who helped me to organize all different kinds of things and for advising me in various matters: Dr. Katharina Achazi, Dr. Wiebke Fischer, Dr. Jens Dernedde, Eike Ziegler, Jutta Haß, and Dr. Pamela Winchester who deserves special thanks for help at very short notice.

Furthermore, I would like to thank all my cooperation partners and the administration of the SFB 1112 and the DRS. Special thanks go to the proof-readers Dr. Katharina Achazi and Mathias Dimde.

Thanks also go to Prof. Jin Chang and his coworkers for the chance to have a short lab exchange in Tianjin.

I very much appreciated the time spend with my colleagues of the “Lunch Group” and the “Kuchenkolloquium.”

A very special thank you goes to my family and my Fiancé who have supported me during my academic studies.

Table of Contents

1 Introduction

1.1 Nanoparticles

We have contact with a plethora of different nanoparticles in everyday life. Examples are emulsions in cosmetics, light reflection titanium dioxide in sunscreens, quantum dots in flat screen television devices, or even casein micelles in milk.[1-2] These nanoparticles (NPs) are unique in that their size is in the range of 1 nm and 100 nm and can drastically change their properties compared to bulk material. Another promising application for these kinds of particles is drug delivery. This term refers to the process of directing a certain pharmaceutical to the target site thus increasing the local concentration or minimizing systemic adverse effects. The first approaches of this concept were employed in 1952.[3] Starting in the 1980s, nano-sized materials came into the focus of this approach and led to the first FDA-approved nano drug in 1995.[4] When used as drug delivery systems (DDS), they are also referred to as “nanocarriers.” From the application of this nanotechnology emerged the promising field of “nanomedicine.” The unique properties of nanoparticles arise from their special size range, which is bigger than that of smaller drug molecules but small enough to be taken up by cells. Also, this size range makes it possible to encapsulate smaller molecules and be bigger than the renal clearance cut-off. Still, at the same time they are small enough to circulate in the blood stream and invade tissues.

The purpose of NPs in nanomedicine is the amplification of a drug’s bioavailability, either systemic or in specific organs and tissues. The major challenge that needs to be overcome by nanocarriers are biological barriers. Drugs that do not meet the requirements of the Lipinski rule of five usually are too hydrophilic, too lipophilic, just not stable enough in a biological environment to reach a high enough concentration at the target site, or they have short circulation time due to a fast clearance.[5] To address these weaknesses, nanocarrier systems often serve to load, encapsulate, or couple a drug and overcome the respective weakness.[6] The complexity of the carrier system can be increased with a trigger mechanism for the drug release or a targeting moiety for the selective transport to a certain tissue or environment. Among these nanocarriers, cationic particles play a special role as they have unique interactions with cell membranes, negatively charged biomolecules, and lysosomes. Different types of nanocarrier systems and their mode of action as well as their drawbacks will be elucidated in the upcoming chapters of this work.

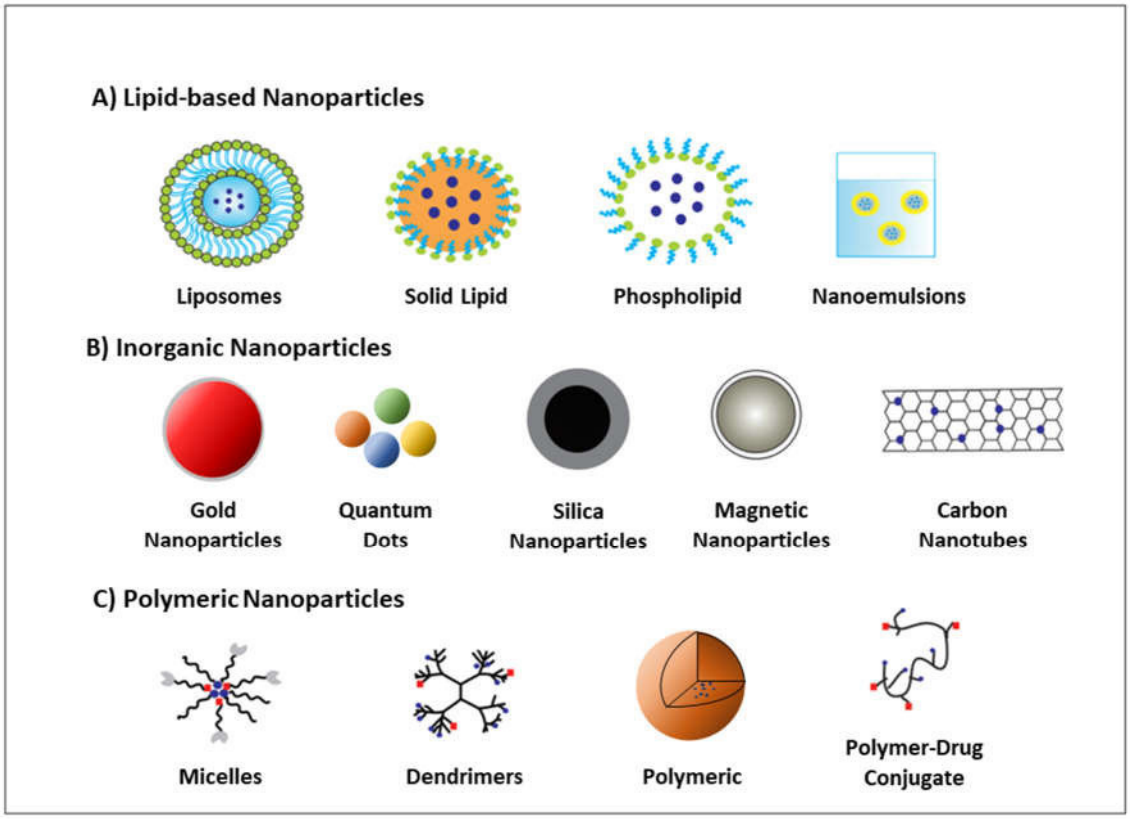

Figure 1. Overview of commonly used nanoparticles. Picture modified with permission from [6].

As there is a manifold of applications for nanocarriers, different kinds of materials that can be utilized. A rough classification of different particles based on the used material is shown in Fig. 1: lipid-based, inorganic and polymeric nanocarriers. It should be noted that different material classes can be combined with one another. This is especially true for the inorganic nanoparticles, as they are often modified by polymers or biomolecules for biological applications.[7-8]

The defining property of lipid-based particles is the co-existence of a lipophilic and a hydrophilic compartment. Liposomes consist of a membrane bilayer that encapsulates an aqueous compartment, whereas micelles form a single membrane that encapsulates a lipid compartment. Nano emulsions are a biphasic dispersion of water in oil or oil in water, utilizing an amphiphilic surfactant. Solid-lipid nanoparticles derive their name from a solid lipid core, which has been stabilized by a surfactant. The basic principle is always that the desired cargo is transported according to its properties, either in the lipid or aqueous compartment. Furthermore, a variety of different amphiphilic compounds can be used and modified to fulfill specific application requirements.[9-11].

Inorganic nanoparticles, sometimes called “hard nanoparticles”, have their own unique properties among nanoparticle systems. Owing to their optical properties, gold NPs and quantum dots are versatile tools for bioimaging and used for diagnostics as well as photothermal therapy.[12-13] Mesoporous silica particles are one example of drug delivery systems purely based on inorganic nanoparticles, as poorly water-soluble drugs can be transported in their pores.[14] Also carbon nanotubes have been applied for drug delivery to a certain extent,[15] while magnetic nanoparticles are used to induce magnetic hyperthermia in order to fight cancer.[16] Some major drawbacks of most inorganic particles are their inherent poor solubility in water and their stability against degradation inside of biological systems. Like lipid-based nanoparticles, inorganic ones are often further decorated by polymers or biomolecules in order to optimize their performance.

Polymeric nanoparticles can be produced from a plethora of different polymers ranging from polysaccharides like chitosan and alginate to synthetic ones.[17-18] The abundant list of possible synthetic polymers includes, among many others, polystyrene, polyacrylates, polyethyleneimine (PEI), polyethylene glycol (PEG), or polyglycerol (PG).[19-23] Similar to lipid-based nanoparticles, the particulate structure of the polymers can be micelles. For this purpose, amphiphilic block copolymers are used, which consist of a core and a shell. A direct coupling of the drug to one polymer yields a polymer-drug conjugate in which the combined molecule has the beneficial properties of both ends. The branched polymer structure is called dendrimer because it has a tree-like shape. Each layer of monomers in these molecules is called a generation and they can be made into very defined structures by controlling them. Drugs can be transported via host-guest interactions or by coupling to the end of the branches. More complex systems consist of a dendritic core that has one or more layers of different shells attached to it, which further increases the options for modifications.[24] One last big application for polymers is the formation of nanogels. These are hydrophilic crosslinked polymer networks that can load the drug in their pores or encapsulate them during the fabrication. Additionally, polymers are often used to modify the surface of inorganic nanoparticles.

While the base material for a designed drug carrier system plays an important role, the surface of a nanoparticle is of particular interest for biological applications as this is where the initial interaction takes place. These interactions include contact with the innate or acquired immune system, cellular membranes, or the individual extracellular matrices depending on the application. In this context, the surface charge of a particle is one of the major characteristics that determine the course of these interactions. Condensed, a neutrally charged particle has few interactions with cellular membranes compared to negatively charged particles that can interact to some extent via electrostatic interactions.[25] Positively charged ones showed strong interactions with biological

membranes due to the interactions with the negative groups on the cell surface.[26] The upcoming chapter will elucidate the benefits and applications of cationic nanoparticles as the focus of this work.

1.2 Advantages and Applications of Cationic Nanoparticles

1.2.1 Enhanced Cellular Uptake and Endosomal Escape

In order to highlight the benefits of cationic nanoparticles enhanced cellular uptake, a brief overview of different cellular uptake mechanisms needs to be introduced first. In general, the two major ways of endocytosis of nanoparticles are phagocytosis and pinocytosis. Phagocytosis is a distinctive ability of immune cells such as macrophages which ultimately leads to the cargo being transferred to the phagosome which in turn fuses with lysosomes.[27] Pinocytosis as the ubiquitous uptake pathway can be further classified according to the involved subcellular structures.[28] One important pinocytosis mechanism is termed after the invagination and vesicle coating structures, clathrin-mediated endocytosis (CME). This pathway plays a role in the uptake of big molecules such as insulin and growth factors but also has been described for the uptake of particles with a size of up to 200 nm.[29-30] Caveolin-mediated endocytosis (CvME) is another prominent route for nanomaterials. These flask-like invaginations are coated with caveolins and have a diameter of 60 nm to 80 nm.[31] Nanoparticles with sizes of up to 40 nm seem to be favorably taken up but also 100 nm particles can be transported with this pathway.[32] Particles with sizes of up to 1 µm can be internalized by macropinocytosis. This route is unspecific but has a high capacity, making it an important part of nanocarrier mediated drug delivery.[28] The three described pinocytosis pathways are dependent on the scission of vesicles by dynamin.[33] There are, however, a plethora of other pathways that are not necessarily dynamin dependent under active investigation.[34-35] Noteworthy, none of these uptake pathways are exclusive as nanoparticles are usually taken up by all of the mentioned ones to some degree, even though one of them might be favored. Also, which pathway is favored has been demonstrated to be cell line specific. [36] Diaz-Moscoso *et al.* demonstrated that cationic cyclodextrin nanoparticles were predominantly taken up by CME, whereas a successful transfection was only possible via clathrin-independent uptake.[37]

Despite these canonical uptake pathways, cationic NPs have certain unique interactions on the cellular level that are often exploited for drug delivery applications. One of their qualities is the strong direct interaction with biological membranes via electrostatic

interactions of its positive terminal groups and the negative phosphate groups of the membrane or protruding groups like sialic acid. Fig. 2 illustrates the local changes of the membrane upon contact. While detrimental effects like membrane restructuring and leakage due to pore formation occur, the strong interaction opens up the possibility for passive membrane translocation (Fig. 2 C) as an additional uptake mechanism. This process has been demonstrated by Le Bihan *et al.* [38] using liposomes to be independent of supplementary energy. Another study showed that positively charged gold particles could penetrate a lipid membrane as well as dwell in the hydrophobic phase of the lipid bilayer, while negatively charged particles did not do that.[39] Having the option to directly penetrate the membrane and circumvent lysosomal uptake makes cationic particles a promising contact with membranes and also increases the uptake rate of canonical endosomal pathways. Harush-Frenkel *et al.*[40] demonstrated that positively charged particles have a higher rate of uptake via the clathrin-mediated endocytosis (CME) compared to negatively charged ones. Also, when CME is blocked, a compensatory alternative endocytosis pathway is activated. Similar observations were made by Chung *et al.*,[41] when mesoporous silica particles with a high surface charge were applied on mesenchymal stem cells. While CME and micropinocytosis are the most common cellular uptake pathways for nanoparticles, polycations like PEI have been demonstrated to also enter the cell via caveolae-mediated endocytosis.[42]

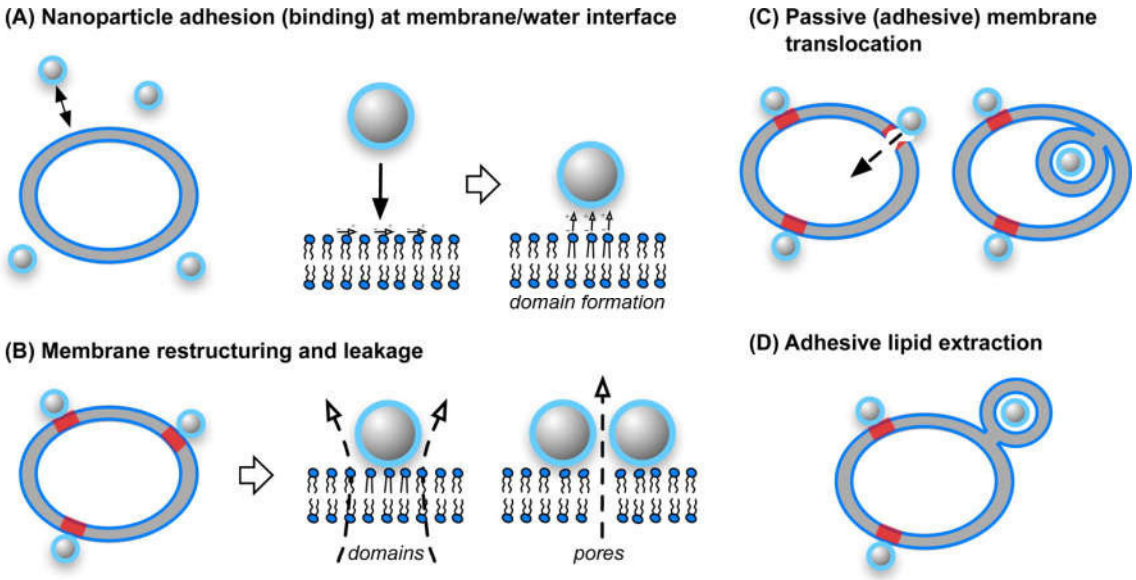

Figure 2: Interactions of nanoparticles and membranes. The red regions indicate local membrane changes. Adapted with permission from [43].

Apart from the membrane penetration, particles that are taken up by endocytic pathways as CME, micropinocytosis and to some extent caveolae-mediated uptake [44] will be transferred to the endosome, which in turn is further processed to the lysosome. In this compartment, the pH value drops to 4.5 – 5.0.[45] At this point, the appeal of polycationic carrier systems lies in their dual function of both protecting the drug from degradation and escaping from the lysosome so that a drug can be released into the cytosol. An explanation for this is given by the "proton sponge" hypothesis in Fig. 3.

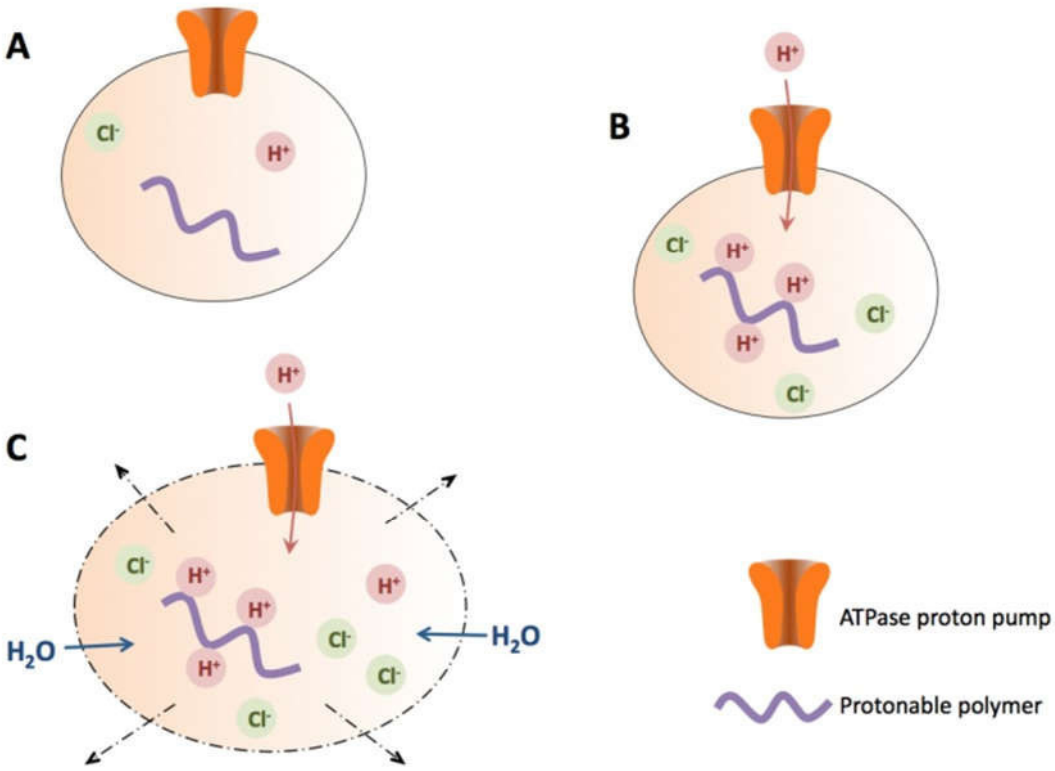

Figure 3. Proton-sponge hypothesis mechanism. Figure adapted with permission from [46].

During the maturation of the early endosome, the pH value of the lumen is gradually decreased by membrane-bound ATPase proton pumps.[47] Simultaneously, chloride ions are transported into the lysosome, which increases the osmotic pressure. The poly-cationic particles provide amine groups, lysine, histidine, or other basic groups, which are protonated so the pH value does not sufficiently drop. As more and more chloride ions are pumped into the lysosome and water follows, the pressure gets too high and the membrane will rupture.[46] In recent years, studies have demonstrated that the pH value does not actually change in the presence of polycations, which indicates that

another mechanism plays an important role in the lysosomal escape.[48] Other groups have stated that, on the one hand, the increased tension of the swollen membrane makes it more vulnerable for direct disruption by the polycations. On the other hand, the disruptive effect of the cations is increased by a stronger degree of protonation compared to physiological pH values.[49-50]

1.2.2 Complexation of Nucleic Acids

Condensed, polycationic nanoparticles excel at cellular uptake via passive and active mechanisms while, at the same time, facilitating endosomal escape into the cytosol, potentially via the proton sponge effect. The first molecule to be advertised as a proton sponge was published in 1971 by Gerson *et al.*[51] Although this was a small molecule, proton sponges in the current state of nanomedicine are usually nanoparticulate structures that can complex into bigger drug cargo molecules. There are other applications as the transport of heparin in ulcerative colitis,[52] the most widely used class of anionic drugs are nucleic acids (NAs). They are very attractive cargo candidates, because they possess a lot of negative charges due to their phosphate backbone. Also, they lack the inherent ability to penetrate membranes or enter cells because of their large size and their negative charge. One way to use NAs as a therapeutic agent is gene therapy. Here, a plasmid DNA is transferred into the host cells in a process that is called transfection. The introduction of plasmid DNA to a cell enables it to express encoded genes that might be defective in its own genome.[53] With this approach it is possible to treat genetic disorders such as hereditary diseases, as was successfully demonstrated in 2000.[54] Meanwhile, studies have proven success *in vitro* and *in vivo* with polymeric cationic nanocarriers using materials like poly-lactic acid or polyethyleneimine.[55-57] Nowadays, polymeric particles replaced viral vectors as promising approaches due to the intricate safety issues of the latter. Still they are not without risk as they require strategies to circumvent the high inherent toxic potential of materials with a high cationic charge like PEI.[57]

A different approach of NA transfection by cationic nanoparticles is the use of microRNA (miRNA) or small interfering RNA (siRNA). These variants of NA do not express a gene but rather inhibit the expression of a gene. Unlike plasmid DNA that needs to enter the cell nucleus, siRNA and miRNA work while being in the cytosol, thus bypassing the hurdle of the nuclear membrane. On the other hand, RNA molecules tend to have a much lower *in vitro* and *in vivo* stability due to ubiquitous nucleases.[58] Briefly, in the case of the siRNA mechanism, a double-stranded RNA is cleaved by an endoribonuclease

dicer generating siRNA as a template to recognize complementary mRNA. Together with intracellular proteins, it forms the RNA-induced silencing complex (RISC). The RISC then uses the template siRNA to bind to the mRNA of the cell and cleave it, which leads to the mRNA degradation and an inhibition of the gene expression (Fig. 4 A).[59] This type of NA for therapeutic use has first been successfully applied by Leachman *et al.* in 2008 on humans using naked siRNA.[60] This study used intra-lesional injections into the skin. Since then, a lot of nanoparticles for systemic application of siRNA have been invented, *inter alia*, cationic ones using polymers such as PEI.[20, 61]

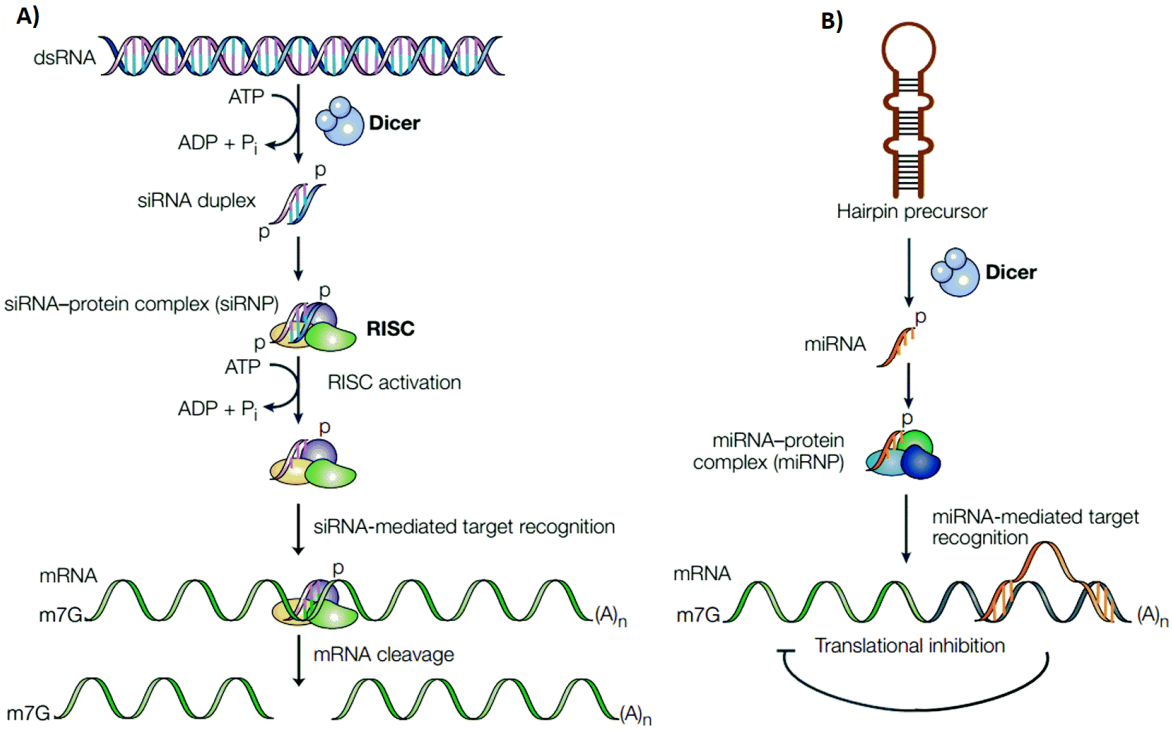

Figure 4. Mechanisms of RNA interference. (A) siRNA mechanism and (B) miRNA mechanism. Figure adapted with permission from [62].

Another commonly used small NA for a gene-silencing application is microRNA, which acts in a similar way to siRNA (Fig. 4 B). This has a hairpin structure that, upon cleavage by the endoribonuclease dicer, generates a single-stranded RNA fragment. This fragment is incorporated into the RISC (sometimes called miRNA-protein complex) and can lead to either cleavage of the complementary mRNA or inhibit the translation process.[63] MicroRNA has similar weaknesses as siRNA, which is why a nanoparticle carrier system seems beneficial. Successful *in vivo* studies have been performed using polymeric particles like poly(lactic-*co*-glycolic acid), albeit with the help of the cell-

penetrating peptide penetratin.[64] Cationic particles using PEI have also shown good results *in vivo* by inhibiting the function of cancer stem cells.[65]

Highlighting the benefits of cationic nanoparticles, they seem to be a very promising delivery platform for drugs. When made of polymeric material, they are easier to produce on larger scales. [66] Furthermore, viral vectors have inherent problems of immunogenicity and thus are arguably more inferior drug delivery systems than polymeric nanoparticles. Furthermore, the high positive charge enables them to complex different kinds of nuclei acids, a promising class of drugs that is both prone to degradation and has very limited abilities to reach the target sites on its own. Not only do cationic nanoparticles complex NAs, they also facilitate their cellular uptake and endosomal escape, respectively.

However, since the early days of their biological application, particles with a high positive charge have been subject of debate. The reason for that is that with the positive charge density comes a high potential for toxicity at various target sites. For this reason, cationic nanoparticles like PEI have been regarded with caution.[67-69] For that reason, many different strategies have been used to fine tune the physicochemical properties of nanoparticles such as size, shape, charge, surface functionalization, and degradability for better delivery effects and lower toxicity. The upcoming chapter of this work will explain the various target sites and toxic effects that need to be addressed by these tuning processes.

1.3 Adverse Effects of Nanoparticles

1.3.1 Systemic Effects

Adverse effects are effects that are not wanted in the course of a treatment,[70] in the case of nanoparticles an adverse effect represents cellular or systemic toxicity. Adverse Effects that nanoparticles have on biological systems such as the mammalian body can occur at different time frames. The course of effects is dictated by the pharmacokinetic ADME principle.[71] On a smaller scale, this principle can be utilized to tailor particles and predict their effect on the cellular level.[72] The central points of that is that any pharmacological effect is dictated by **a**bsorption of a drug by the body. The same point is important *in vitro*, as the amount and the way a particle is taken up into a cell does influence its efficacy and toxicity as the effective dose increases.[73-74] The **d**istribution

inside of the organism or cell is the next important factor. The previous chapter of this work elaborated the possibility of cationic nanoparticles to enter the cell via different mechanisms*, inter alia*, via direct membrane translocation, CME or caveolae mediated endocytosis. The latter uptake pathways direct the particle to a different compartment with different environmental conditions: the cytosol, the lysosome or the caveosome, respectively. The **m**etabolism, in this context the biodegradability of a nanoparticle, plays an important role as well. Degradable particles are more easily excreted by the body via renal clearance and have a shorter intracellular retention.[75-76] The last point is the **e**xcretion. This one is important as a long retention time inside of a cell is connected to a higher toxicity.[77-78] Summarizing, adverse effects are unwanted effects of a nanoparticle system and there are several starting points to tweak that system to minimize these effects: absorption, distribution, metabolism and excretion. To this day, a variety of different adverse effects on the systemic level, in specific tissues, and on the cellular level have been reported.

One well documented source of small particle mixtures that also contain harmful nanoparticles is ambient air. These are classified according to their size as particulate matter with a size below 10 µm (PM_{10}) and 2.5 µm ($PM_{2.5}$) respectively.[79] As the first studies of these airborne particles identified their size in the nanometer range as a key feature to induce toxicity, they formed the concept of nanotoxicology.[80] Although the primary exposure route is the respiratory tract, effects on the cardiovascular system and systemic inflammation have also been observed, followed by cellular uptake and transcytosis across endothelial and epithelial cells into the blood and lymph circulation. Choi et al. demonstrated that non-cationic nanoparticles can rapidly transfer to the lymph nodes and the blood stream depending on their size, whereas the smaller ones (< 6 nm) were also cleared by the kidneys rapidly. Cationic ones however did no penetrate the lung epithelia.[81]

Another important site of nanoparticle exposure are cosmetics that are applied on the skin, being the largest organ of the human body. In general, nanoparticles that have a high exposure on skin such as titanium dioxide or silver in sunscreens and cosmetics do not significantly penetrate intact human skin. Uncertainties do arise though when the barrier function of the skin is impaired by damage, so that particles could be found in the dermis of pigs.[82] One increasingly rare condition is the grey to purple discoloration of the skin called argyria, which can occur upon uptake of silver nanoparticles and subsequent silver deposition in the basal lamina of the skin, also after oral absorption.[83]

After the absorption in the respiratory tract through the air, in the gastrointestinal tract through food, or via the transdermal route on damaged skin, nanoparticles will

enter the blood stream and pass the liver. Here, they will be subject to drug metabolism by liver enzymes.[84] Also, nanoparticles often accumulate in the liver, causing local damage and inducing systemic side effects.[85-86] The primary mechanism for this damage is the generation of reactive oxygen species and the activation and autophagy of the liver resident macrophages, the Kupffer cells.[87-88] These cause acute inflammations and drive apoptosis. The same mechanism applies in other clearance organs that take part in the mononuclear phagocyte system (MPS) such as the spleen and the kidney. Consequently, the interaction with these clearance tissues and macrophages is of great interest as 95% of all non-degradable nanoparticles are estimated to accumulate there.[89] Knudsen et al. also observed accumulation and DNA damage caused by cationic liposomes in the lung and spleen of rats at higher doses. This effect could also be observed for micelles at the highest concentration.[90]

Subsequently, the most common adverse effects on the cellular level such as membrane disruption, generation of reactive oxygen species and genotoxicity will be discussed with a focus on cationic nanoparticles.

1.3.2 Cellular and Subcellular Mechanisms

In vitro, an adverse effect implies a decrease in cell viability. Cell viability is the ability of a cell or cell population to carry out a specific function.[91] As cells are complex biological systems there are several possible interference points. The outmost one is the cell membrane, a lipid bilayer that separates the inside of a cell from the outside. This is a common target site of cationic nanoparticle toxicity. A disruption of the cellular membrane leads to leakage of the cellular compounds. Physiologically, this happens frequently, especially in tissues with a high mechanical stress such as muscles or blood vessels.[92] This is tolerable because cells are able to reseal the cell membrane via several different mechanisms such as tension reduction by reorganization of actin filaments or by exocytosis of intracellular vesicular compartments like endosome and lysosomes as a membrane supply.[93] Chen *et al*. demonstrated that even at subtoxic concentrations cationic nanoparticles were able to induce nanoscale effects of the membrane ranging from 1 nm² to 350 nm². Furthermore, the defect forming events took 1 ms to 100 ms, which is much faster than the repair in the tested cell lines that took several seconds.[94] Figure 2 (page 5) displays the interaction between nanoparticles and membranes. When the particle adheres to the membrane, e.g. by electrostatic interactions, it can induce lipid restructuring, domain formation and local deformation.[95] Li *et al.* found out that

these can then lead to void or pore formation due to an increased membrane surface tension, likely caused by steric crowding of cationic polystyrene nanoparticles.[96-97] Theoretical models have shown that in order to form pores in a membrane, the surface tension needs to me high enough indicating that in drug delivery application the buffer capacity of a particle is an important factor for endosomal escape and effective nucleic acid delivery.[98] As it stands, the transfection efficacy of NA's by cationic nanoparticles and their toxicity are like related.[99-100] This is plausible as the ability to overcome membranes both enables endosomal escape and leads to pore formation in the cell membrane, causing a loss in cell viability. Another important point is that for this kind of interaction, the core material is of little interest as only the surface functionality dictates the effect on membranes.[101] Considering these two opposite requirements for nanoparticle delivery systems, low surface charge for high cell viability but high surface charge for efficient transfection, a fine charge tuning during the synthesis is necessary to find the optimal balance.

A second mode of cytotoxicity that is being explored as one of the major mechanisms is the generation of oxidative stress. In general, this term describes the generation of reactive oxygen species (ROS) and reactive nitrogen species (RNS). An overview of ROS and their connections is given in Figure 5. The superoxide radical $O_2^{\bullet-}$ presents the primary ROS which will subsequently interact with other molecules, either directly or catalyzed by enzymes and metals. As a protective mechanism, three variants of the enzyme superoxide dismutase (SOD) are employed. Intracellular SOD1 and extracellular SOD3 use copper and zinc as their cofactor whereas mitochondrial SOD2 uses manganese.[102] They facilitate the conversion of the superoxide to oxygen via reduction of the metal cofactor (Cu^{2+} or Mn^{3+}) or to hydrogen peroxide:

$$O_2^{\cdot-} + O_2^{\cdot-} + 2H^+ \rightarrow H_2O_2 + O_2 \quad or \quad M^{(n+1)+} + O_2^{\cdot-} \rightarrow M^{n+} + O_2 \qquad (1)$$

Although two radicals are eliminated in this reaction the very reactive hydrogen peroxide molecule is formed which can lead to the generation of further radicals. H_2O_2 can be further decomposed to hydrogen peroxide and oxygen by the enzyme catalase.[103] This is a two-step reaction where in the first step the hydrogen peroxide oxidizes the heme and forms a porphyrin cation radical in the enzyme (E) with an oxoiron(IV) intermediate species, Eq. 2. This intermediate is stabilized by the protein environment.[104] In the second step another hydrogen peroxide is oxidized and that regenerates the heme-containing catalase, Eq. 3:

$$H_2O_2 + Fe^{3+}{-}E \rightarrow H_2O + OFe^{4+}{-}E^{\cdot+} \quad (2)$$

$$H_2O_2 + OFe^{4+}{-}E^{\cdot+} \rightarrow H_2O + Fe^{3+}{-}E + O_2 \quad (3)$$

Another physiological protection mechanism against H_2O_2 is reduced glutathione (GSH) that can be utilized by glutathione reductases. These enzymes used glutathione as a substrate that is converted to its oxidized form GSSG:

$$2GSH + H_2O_2 \rightarrow GSSG + 2H_2O \quad (4)$$

Afterwards the oxidized GSSG will be regenerated by the glutathione reductase via oxidation of reduced nicotinamide adenine dinucleotide phosphate (NADPH).[105] Catalase and peroxidase work in unison on the H_2O_2 degradation, whereas GSH reductase plays a more important role at low concentrations while catalase is important for higher H_2O_2 concentrations.[106]

Despite these protective mechanisms, a portion of the generated ROS reacts in different ways that are harmful to cells. This is especially true when the generation of ROS due to the influence of nanoparticles is increased. That way, superoxide can bind to the radical nitric oxide to form peroxynitrite, which is a strong oxidant.[107] Hydrogen peroxide is a reactive molecule as well that can form the very reactive hydroxyl radical $OH^{\cdot}$. This reaction in Eq. 5 is called the Fenton reaction, in which iron(II) is oxidized to form the hydroxyl radical and hydroxide ion.[108] In the Haber Weiss cycle, superoxide reduces iron(III) back to iron(II), so that the Fenton reaction can happen again. This nets the bottom Eq. 6 below, in which superoxide and hydrogen peroxide form the hydroxyl radical.[109]

Fenton reaction: $H_2O_2 + Fe^{2+} \rightarrow Fe^{3+} + OH^- + OH^{\cdot}$ (5)

Haber Weiss reaction: $O_2^{\cdot-} + H_2O_2 \rightarrow OH^{\cdot} + OH^- + O_2$ (6)

The hydroxyl radical can further react with molecules such as proteins to form alkyl ($R^{\cdot}$), alkoxyl ($RO^{\cdot}$) and alkylperoxyl radicals ($ROO^{\cdot}$) in living systems.[110]

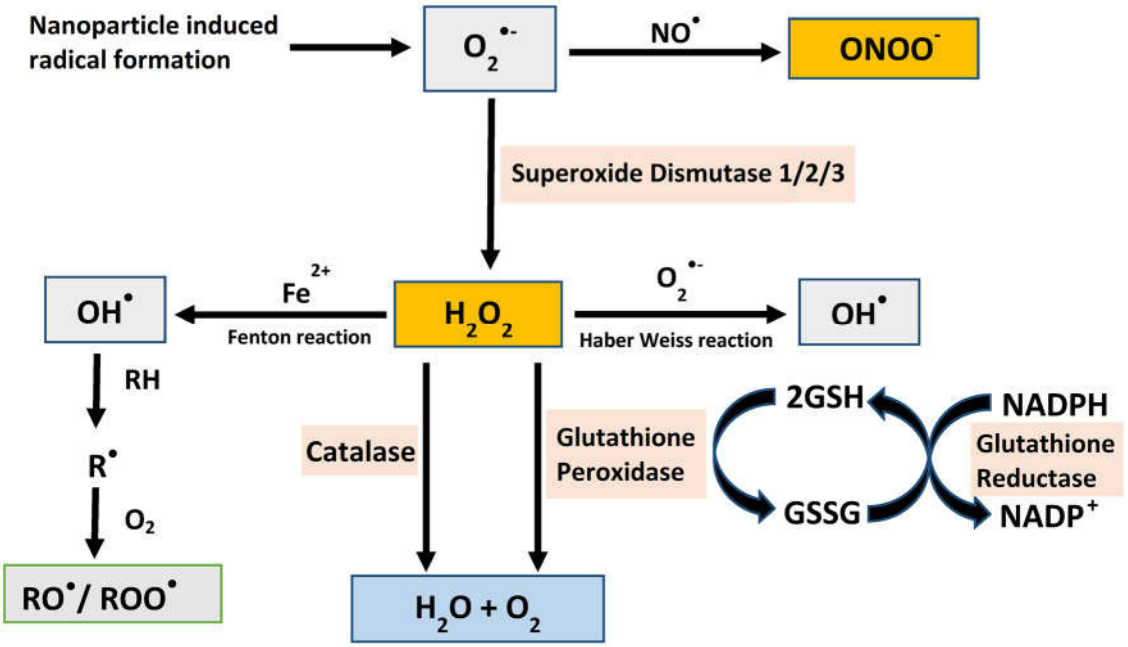

Figure 5. Pathway of reactive oxygen species in cells. GSH, glutathione; RH, lipid membrane; R, alkyl radical. Figure modified with permission from [111].

The reason why oxidative stress is considered one of the main mechanisms of nanoparticle induced toxicity is that upon generation of ROS, all components of a cell from lipids to proteins to nucleic acids can be damaged, leading to a plethora of detrimental effects.[112] At biological membranes, reactive oxygen species induce lipid peroxidation. Herein lipoperoxyl radicals are formed from unsaturated fatty acids ($LOO^{\cdot}$). These can then react with a lipid, resulting in a lipid radical and a lipid hydroperoxide (LOOH).[113] As these are unstable, they produce further radicals and decompose to secondary products. The aldehyde secondary products are such as malonaldehyde and 4-hydroxynonenal (4-HNE) are of interest as lipid peroxidation markers for biological examinations.[114] Van der Paal *et al.* could show through simulation that the generation of these marker molecules increases disorientation in the membrane, making it more prone to pore formation.[115] Another important point for toxicology is the ability of these aldehydes to bind DNA and form adducts, leading to genotoxicity.[116] 4-HNE has further been found to bind and alter histones, changing its confirmation and increasing the vulnerability of the DNA.[117]

Similar to lipids, protein oxidation is a common effect of ROS generation. There are several attack points for radicals such as alkylperoxyl (ROO$^{\cdot}$) and alkoxyl radicals (RO$^{\cdot}$). One is the α-C-atom of the protein backbone which will be converted to a carbon-centered radical. This can react with other backbone radicals to form protein crosslinks or the peptide bond can be cleaved, both resulting in loss of function of the protein.[118] Another mode of action is the oxidation of the amino acid residues, whereas amino acids with aromatic side chain groups and sulfhydryl groups are the most sensitive ones.[119-120] The modification of these groups can cause a loss of function and crosslinking via disulfide bonds. Also, protein carbonyl groups can be formed that will further bind to α-amino groups of lysine residues. This kind of crosslink can lead to the formation of protein aggregates which are resistant to degradation mechanisms and thus inhibit proteolytic processes and accumulate.[119]

Nucleic acids such as DNA and RNA can also be altered by ROS due to oxidation of the DNA/RNA bases. There have been around one hundred different base lesions identified in model studies.[121] One ubiquitous base oxidation product is 8-oxoguanine which is formed from guanine via oxidation by hydroxyl radicals (OH$^{\cdot}$) and another important one is 7-methylguanin that is formed by alkylation.[122] Guanin, purine and pyrimidine can also form interstrand crosslinks.[123] RNA as another nucleic acid is affected to similar lesions as DNA albeit with higher levels. This can be attributed to the fact that RNA is mainly single stranded and thus more accessible, has extensive cytoplasmatic distribution and is in proximity to mitochondria.[124] Crosslinking of nucleic acids can also occur not only intracellularly but also with lipids and proteins in the presence of ROS.[116, 125] As mRNA is a molecule with a limited lifetime, lesions causing RNA damage will hinder the protein synthesis and impact the cell homeostasis. Damage to the DNA, however, can lead to genotoxicity when cellular repair mechanisms fail. Genotoxicity, mutagenicity and cancerogenicity and the underlying mechanisms are broad issues that are beyond the scope of this work, so the entire subject will only be broached.

Briefly, genotoxicity describes the ability of a substance to damage the DNA. These damages can be repaired by cellular repair mechanisms, however, they have a small intrinsic an error rate. If one of these errors occur or if the damage was not repairable, the genetic material can be altered.[126] This alteration is called a mutation so substances that cause them are considered mutagenic, possibly resulting in apoptosis.[127] A mutation in a germ cell may lead to infertility or diseased offspring or daughter cells if non-lethal to the cell. Mutations in somatic cells on the other hand may lead to cancer, thus called cancerogenicity.[128] So, a substance such as a reactive oxygen species or its derived lipid radicals or protein radicals can be all of the above, mutagenic and genotoxic or just genotoxic. A nanoparticle inducing ROS in a cell that subsequently causes DNA

damage is considered a secondary genotoxin.[129] As previously elaborated, ROS can induce the alteration of DNA in the form of alkylation, oxidation, adducts and crosslinks. These altered sites can be repaired by several repair mechanisms such as base excision repair, nucleotide excision repair, mismatch repair, interstrand crosslink repair and repair of single and double strand breaks.[130] However, they can also lead to different types of DNA mutation in the repairing process. One variant is point mutation, where effectively one base is replaced by another one. These can be without effect (silent) as some codons code for the same amino acid during translation of the mRNA or the occur in in non-coding regions. They can also lead to missense mutation, where a different amino acid is translated or nonsense mutation, forming a stop codon.[131-132] A frameshift-mutation moves the coding frame and thus leads to a completely different protein expressed. On a bigger scale, chromosome mutations due to strand breaks can, inter alia, lead to deletion, insertions and inversions, all of which causing massive interruptions in the respective genes expression.[133]

Taking all the effects of oxidative stress into account, the generation of ROS truly is an imposing adverse effect with all these different manifestations. Still as of today, the exact mechanism of ROS generation by cationic particles remains elusive. Adding difficulty to this issue, Xia et al. demonstrated that cationic polystyrene particles exhibited different effects depending on the used cell line.[134] Macrophages (RAW264.7) and epithelial cells (BEAS-2B) were sensitive to the generation of oxidative stress while endothelial cells (HMEC), hepatoma cells (HEPA-1) and pheochromocytoma cells (PC-12) were relatively resistant. The first two favored a lysosomal uptake route of the particles leading to mitochondrial disruption while the latter ones favored caveolae mediated uptake. However, studies indicated that the interaction of the positive surface charge with mitochondrial membranes plays a key role in this process. Hunter *et al.* presented that both linear and branched PEI could interact with the outer mitochondrial membrane and form pores in T-cells (Jurkat). These pores altered the mitochondrial membrane potential that is necessary for the synthesis of ATP and also lead to a release of cytochrome c and activation of caspase-3.[135] Symonds *et al.* observed comparable effects using poly-L-lysine and furthermore showed that the mechanisms differed between particles of low and high molecular weight.[136]

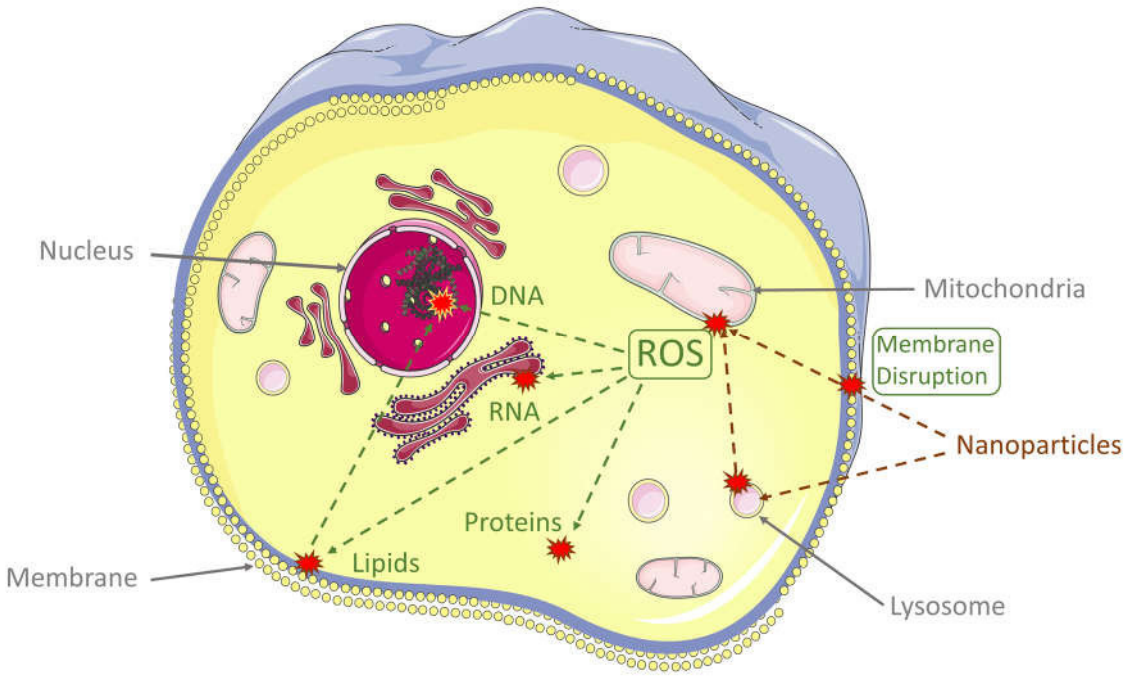

Figure 6. Adverse interactions of cationic nanoparticles with cells. Red stars indicate points at which damage to biological structures is done and where modification of nanoparticle delivery systems will be beneficial.

Figure 6 compiles an overview of the adverse interactions of cationic nanoparticles with cells described in this section. In the first instance, the positive surface charge will interact with the cellular membrane and lead to pore and domain formation. This can lead to leakage of cellular compounds and facilitates the direct penetration into the cytosol. The same interaction helps these particles to escape from the lysosome after cellular uptake and transfer to the cytosol. There, they can interact with the mitochondrial membrane and induce the formation of reactive oxygen species. These will subsequently react with lipids, proteins and nucleic acids, altering or disrupting their function and negatively affect the cell viability. Still, cationic nanoparticles are a promising tool for the delivery of drugs such as nucleic acids. The following section will describe strategies to modify the ADME of different nanoparticle systems increased biocompatibility.

1.4 Strategies to overcome adverse effects

1.4.1 Nanoparticle Materials

Polymeric nanoparticles have a great variety of options for modification in order to change their physicochemical structures. Following basic pharmacokinetic principles, changes after modification will occur either during absorption, distribution, metabolism or excretion. Based on the current knowledge about mechanisms of adverse effects of cationic nanoparticles, it seems obvious that the key parameters are the interactions with the cell membrane, the endosomal membrane and the mitochondrial membrane. Since all these interactions are mediated by their dense surface charge, two strategies have emerged to modify the ratio of delivery efficacy and toxicity: tuning down the surface charge so there is less effects on the membranes and the addition of cleavable moieties to make the particles degradable. Both strategies will be discussed hereafter.

Cationic polymers such as PEI or poly-L-lysine are effective delivery agents because of their high surface charge caused by a high density of amine groups. While this facilitates effective delivery into cells, it is also the primary source of their toxicity. Tuning down the amine group density on the particle surface to a point where the biocompatibility is increased without a loss of delivery efficacy is a promising approach. A polymer that has been explored for this purpose extensively is polyethylene glycol (PEG). This polymer has yielded numerous drug delivery systems that received regulatory approval both in the USA and Europe.[137] One often emphasized advantage of so-called PEGylation is the shielding of surface charge, rendering the particle both less toxic but also less effective for transfection.[138] Also, PEG is used for stealth approaches, meaning that the lower rate of interactions with the immune system increases the circulation time *in vivo*.[139] In summary, the approach of PEGylation decreases the absorption due to lower cellular uptake and slows down the excretion *in vivo* because of a decreased interaction with the reticuloendothelial system (RES) as two key pharmacokinetic parameters. While this decreases transfection efficacy, it increases the biocompatibility. Despite these advantages and approval by the food and drug administration (FDA), several detrimental effects of PEG have been observed. PEG6000 showed genotoxic activity as well as histopathological changes of in livers and kidneys of mice.[140] Also, severe immune reactions could be observed in single cases.[141] Another study by Armstrong *et al.* revealed that pre-existing anti-PEG antibodies in 25 % of healthy blood donors were associated with a rapid clearance of PEG-asparaginase.[142] Richter et al. did not demonstrate antibodies against PEG but indicated PEG-conjugates' potential to function as a haptene

in rabbits.[143] Taking these reports into account, efforts have been made to look for different polymers for biocompatible drug delivery systems.

Among others, one polymer of rising interest is polyglycerol (PG), which has similar possible applications as PEI but so far with no reports for adverse effects. Imran ul-haq *et al.* compared linear PG (LPG) and hyperbranched PG (HPG) to PEG with similar molecular weights. At high concentrations, PEG was demonstrated to decrease cell viability whereas LPG and HPG showed no such adverse effect.[144] Additionally, both PG's had a high circulation time in mice. For food safety, ADME studies showed no accumulation in the body and the European Food Safety Authority (EFSA) concluded that there was no safety concern when used in food packaging.[145] Also, an in depths study by Gerecke *et al*. showed no *in vitro* toxicity of PG based nanogels regarding cell viability, oxidative stress, genotoxicity and irritational potential.[146] Since PG has such a high biocompatibility, it has been employed in different forms for drug delivery applications. One exemplary application is to use HPG that was derived from alkyl chains or methoxy-PEG to form micelles with a hydrophobic core.[147] These hydrophobic cores could load the hydrophobic drugs paclitaxel and docetaxel and effectively kill KU7 cells while not showing cytotoxic effects on their own. Another very sophisticated application using PG is the construction of core-multi-shell structures. The core consists of HPG, the inner shell can be hydrophobic moieties such as alkyl chains of different lengths that serve to load hydrophobic drugs while the outer shell is hydrophilic again, consisting of PEG or PG.[148-149] They have been effective at loading the hydrophobic drug dexamethasone and delivering the dye nile red into the skin at higher efficacy than the conventional cream formulation. Radbruch *et al.* further demonstrated the biocompatibility of these CMS in healthy and inflammatory mouse skin additionally to an *in vitro* biocompatibility array.[150]

For the delivery of nucleic acids, Kainthan et al. have used a PEG-PG composite structure that was modified with quarternary amine groups.[151] This showed superior *in vitro* biocompatibility compared to PEI, whereas the cytotoxic effect increased with the rate of amine functionalization. Zeng *et al.* employed dendritic polyglycerols (dPG) and functionalized them with histidine and tryptophan to mimic the structure of histones. These particles showed good siRNA transfection efficacies with low toxic effects. Furthermore, by varying the ligand density they worked out that a density of 50 % worked the best for 14 kDa cores while 35 % was the best for 55 kDa cores.[152] Further work is required on that topic as both size and surface group density influence the cellular uptake but it is unclear how a bigger size requires fewer surface groups for the best effect.

1.4.2 Biodegradability

A second auspicious approach to overcome adverse effects in cationic nanoparticle drug delivery is to make them biodegradable. While this does not necessarily affect the absorption, it does influence the distribution, metabolism and excretion. Upon degradation the properties of a particle change from that of the whole particle to that of the fragments or degradation products. Depending on the application, the degradation process should start before the uptake, for instance in some anti-cancer drugs that leverage the decreased pH value in tumor tissue.[153] However, if the cargo molecules act intracellularly such as nucleic acids, the degradation should not happen until the particle reached the insides of a cell. While degradable moieties can be beneficial for the biocompatibility aspect of a nanoparticle, they can also be used for passive targeting such as the decreased pH value of tumor tissue or inflamed tissue.[153-154] An overview of linkers that are used in polymeric nanoparticles is given in Fig. 7. Many of these groups are targeting the lysosome. This is the subcellular compartment most likely for the cleavage of these linkers as that is where the pH value drops to 4.5 – 5.0.[45] Furthermore, there are over 50 enzymes located in the lysosome including lipases, nucleases, proteases and esterases that are all activated at these low pH values.[155] When a drug is connected to a polymer, encapsulated or loaded the cleavage of this linker will liberate the drug. It has to be noted that when sensitive cargo such as siRNA is being delivered with this kind of approach, it is likely to be degraded by lysosome enzymes unless it can escape into the cytosol, where the pH value of 7.4 deactivates lysosomal enzymes.[155] Du *et al.* applied the principle biodegradability to the afore mentioned CMS nanocarriers using a polycaprolactone linker. With a core of HPG and an outer shell made of PEG they exhibited a low cytotoxicity *in vitro* and showed an improved skin penetration of nile red compared to conventional creams.[148] Successful gene delivery into the brain was observed after 48 hours using degradable poly(β-amino ester) (PBAE) with a PEG corona by Mastarakos *et al*.[156] Also these particles showed no toxicity *in vitro*. It must be said though that the concentration used for the *in vitro* studies was much smaller than that in the animal studies and the particles were injected directly into the brain. Fischer *et al*. combined dPG with an oligoamine shell for positive surface charge and a biodegradable carbamate linker. This system yielded comparable results to the used positive control HiPerFect when transfecting siRNA. Also, the cytotoxicity was low and comparable to the commercial control.[157]

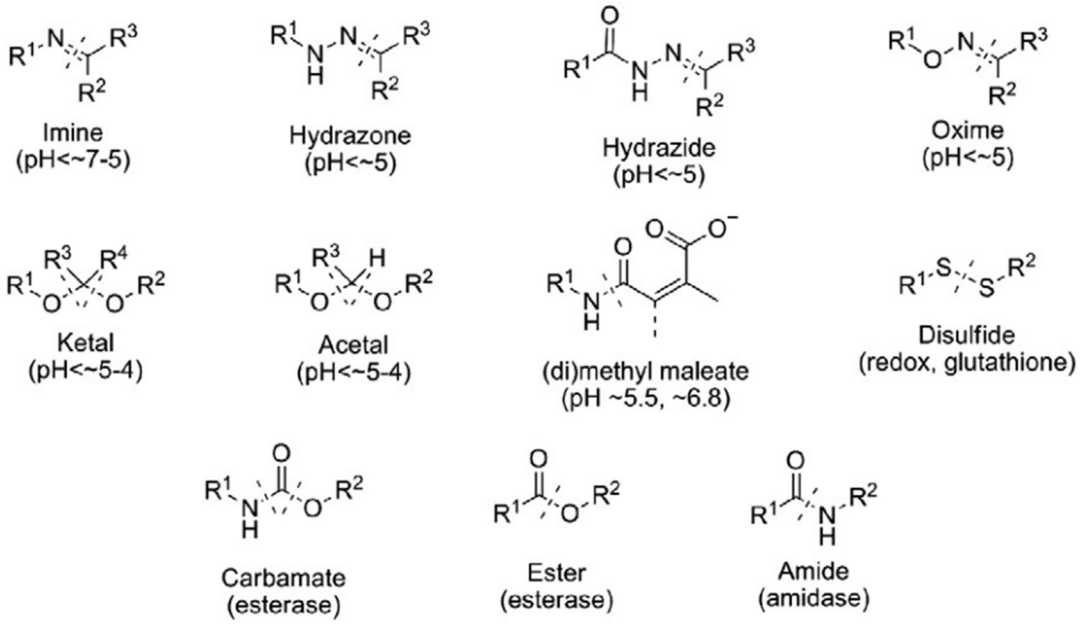

Figure 7: Cleavable linkers used for stimuli-responsive nanocarriers. Dashed lines indicate the bond that is broken upon the respective stimulus, given in parentheses. Figure modified with permission from [158].

In summary, two approaches for the effective use of cationic nanoparticles have been discussed that will have the highest benefit when used in conjunction. Tuning of the surface charge while also using the biocompatible PG as the polymer foundation will decrease the interaction with biological membranes and eliminate the risk of antibody formation or possibility of genotoxicity induced by PEG. As of today, the most effective nucleic acid delivery systems are viral and suffer from health concerns. So, the effort to improve both the transfection efficacy and decrease the adverse effects needs to be made as cationic nanoparticles are still in debate because of their commonly known adverse effects.

2 Scientific Goal

The aim of this work was to further develop strategies for efficient nucleic acid delivery into cells. Fig. 8 shows an overview of the included projects and the strategy that was applied. The overall goal was the development of new cationic PG-based nanocarrier systems for efficient and biocompatible gene delivery. In order to gather more information about the interactions of cationic HPG and transfected cells, an array of different particles with an amine shell of varying degrees of surface functionalization and size was produced. **(1)** The effect of the different sizes and surface charge densities on cells was investigated regarding the parameters of transfection efficacy, cell viability, cytotoxicity and apoptosis induction.

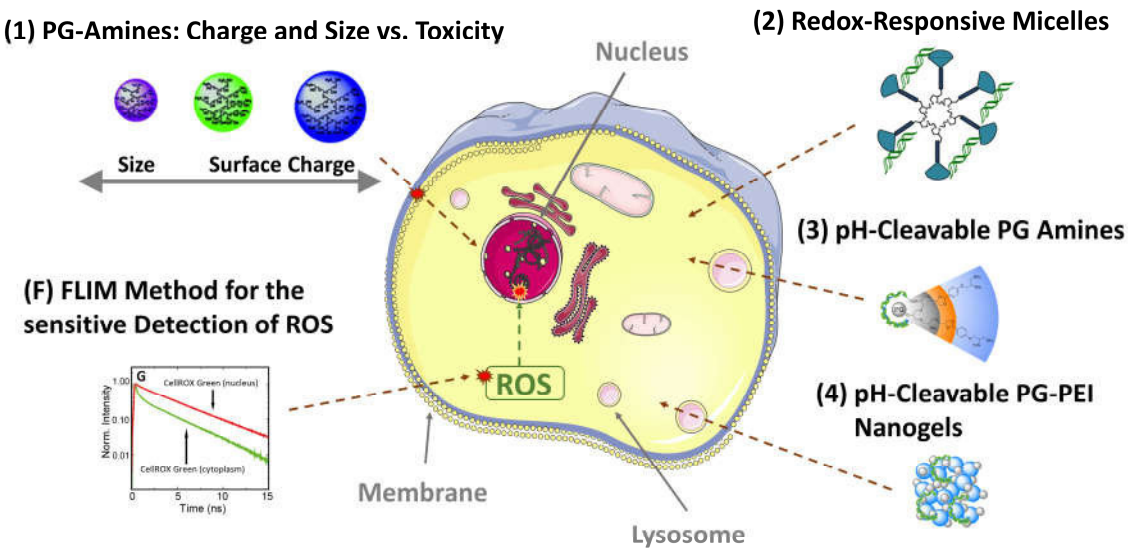

Figure 8: Schematic overview of the scientific projects in the context of drug delivery via cationic nanoparticles.

The second phase consisted of testing three different biodegradable systems with the intent to improve the transfection to cytotoxicity ratio. The first approach was the application of redox-responsive micelles. **(2)** A disulfide linker was incorporated that exploits the increased intracellular concentration of reducing agents such as glutathione compared to the extracellular space. Furthermore, an amine shell was applied that facilitated the transfection process while biodegradability enabled the onsite siRNA

release in the cytosol. Another carrier system comprised dendritic PG, also functionalized with an amine shell. **(3)** In this case, a pH responsive benzacetal linker was incorporated into the nanocarrier system. This was then applied for the successful delivery of GFP plasmid DNA. A third system combined the benefits of PG with that of small 600 Da PEI units. **(4)** While the small PEI by itself does not show sufficient transfection efficacy, the crosslinking with the PG should have led to multivalent presentation of positive charges that disassembled after exposure to the pH trigger.

Another project aimed to establish a method for the sensitive measurement of ROS generated by cationic model nanoparticles. **(5)** Also, a cohesive study of different effects of the cells caused by these particles was performed to elucidate the adverse effect of cationic particle applications and lay the groundwork for further improvements.

3 Publications and Manuscripts

3.1 Systematic Adjustment of Charge Densities and Size of Polyglycerol Amines Reduces Cytotoxic Effects and Enhances Cellular Uptake

Markus Hellmund, Katharina Achazi, **Falko Neumann**, Bala N S Thota, Nan Ma, Rainer Haag*, Biomaterial Science **2015,** 1459-65.

DOI: https://doi.org/10.1039/c5bm00187k

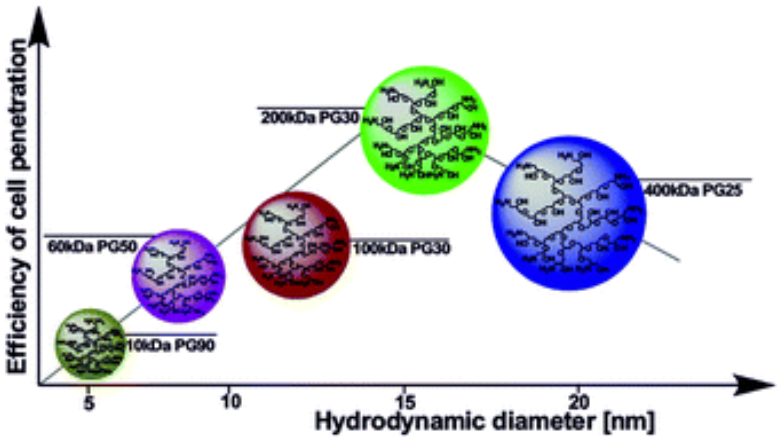

Figure 9: Figure adapted with permission from Hellmund et al.[159]

The contribution of the author was the design of the biological experiments and the evaluation of the transfection efficacies, cell viability, cytotoxicity, and apoptosis. The author contributed parts of the manuscript.

3.2 Crosslinked Redox-Responsive Micelles Based on Lipoic Acid-Derived Amphiphiles for Enhanced siRNA Delivery

Ariane Tschiche, Bala N S Thota, **Falko Neumann**, Andreas Schäfer, Nan Ma, Rainer Haag*, Macromolecular Bioscience. **2016** Jun; 16(6):811-23.

DOI: https://doi.org/10.1002/mabi.201500363

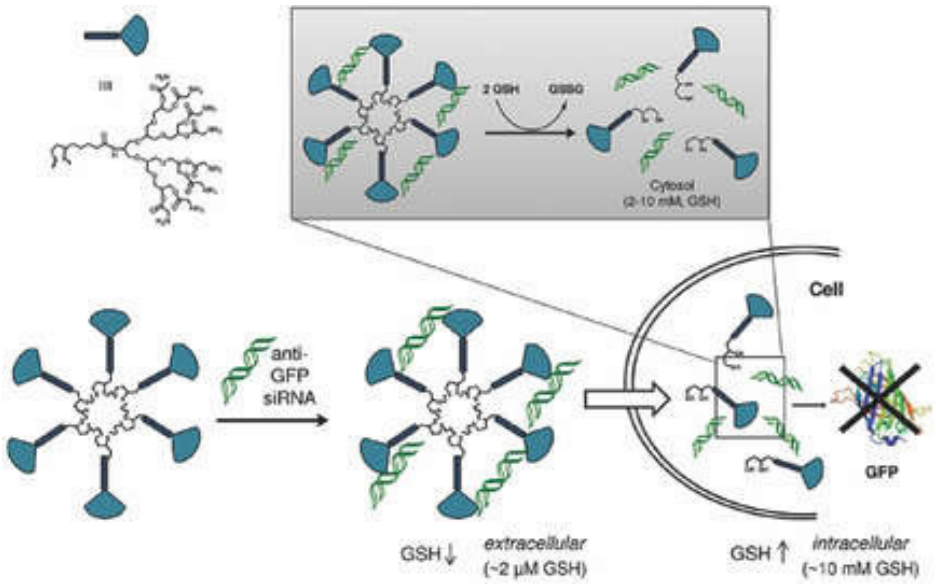

Figure 10: Figure adapted with permission from Tschiche et al.[160]

The author's contribution was the design of the biological experiments and the gene silencing and cell viability studies.

3.3 Synthesis of pH-Cleavable dPG-Amines for Gene Delivery Application

Mathias Dimde, Dirk Steinhilber, **Falko Neumann**, Yan Li, Florian Paulus, Nan Ma, Rainer Haag*, Macromolecular Bioscience. **2017** Jan; 17(1).

DOI: https://doi.org/10.1002/mabi.201600190

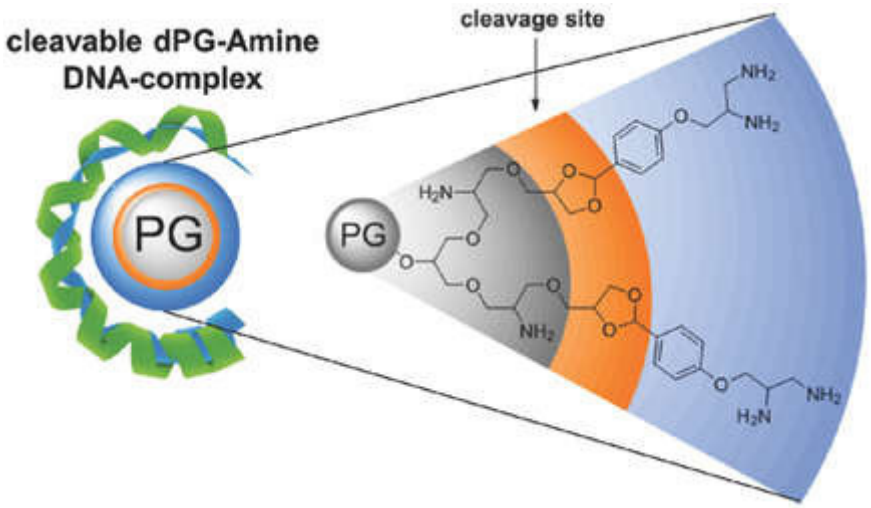

Figure 11: Figure adapted with permission from Dimde et al.[161]

The author's contribution was the design of the biological experiments and the confocal microscopy uptake studies, cell viability studies, fluorescence microscopy images, and transfection efficacy studies. The author contributed parts of the manuscript.

3.4 Defined pH-Sensitive Nanogels as Gene Delivery Platform for siRNA Mediated *in vitro* Gene Silencing

Mathias Dimde[§] and **Falko Neumann[§]**, Felix Reisbeck, Svenja Ehrmann. Jose L C Camacho, Dirk Steinhilber, Nan Ma, Rainer Haag*, Biomaterials Science, **2017**, 5, 2328-2336

[§] Both authors contributed equally.

DOI: https://doi.org/10.1039/c7bm00729a

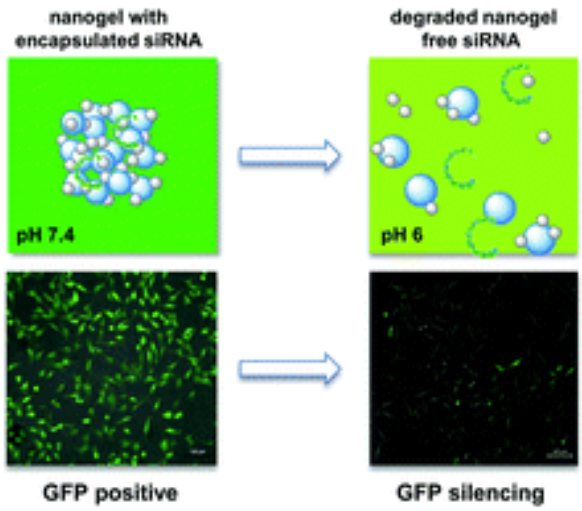

Figure 12: Figure adapted with permission from Dimde and Neumann et al.[162]

The author's contribution was the design of the biological experiments and the cellular uptake, cell viability, and transfection efficacy studies as well as the red-blood-cell lysis assay. The author wrote the manuscript.

3.5 FLIM-ROX as a Highly Sensitive Fluorescence Lifetime Based Approach for Reliable Reactive Oxygen Species Detection *in vitro* and *in vivo*

Jens Balke[§] and Pierre Volz[§] and **Falko Neumann**[§], Robert Brodwolf, Alexander Wolf, Hannah Pischon, Moritz Radbruch, Lars Mundhenk, Achim Gruber, Nan Ma[*], and Ulrike Alexiev[*], **2017**, submitted

[§] All authors contributed equally.

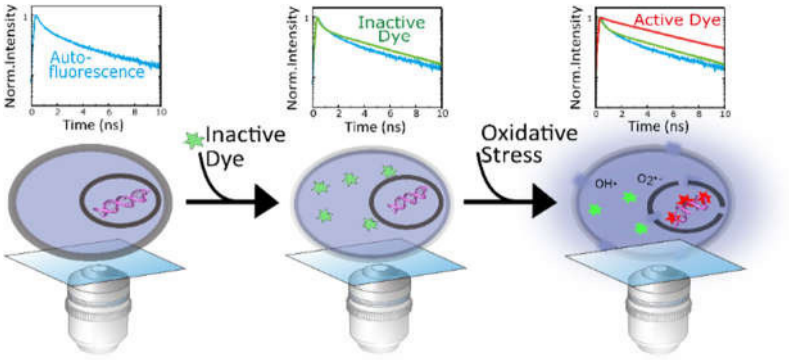

Figure 13: Schematic representation of this project. This image is not yet published.

The authors contribution was the project idea, sample preparation for fixed cells, calibration curves and further cellular studies such as comet assay, senescence assay, cell viability assay and cellular uptake. The author wrote parts of the manuscript.

FLIM-ROX as a Highly Sensitive Fluorescence Lifetime Based Approach for Reliable Reactive Oxygen Species Detection *in vitro* and *in vivo*

Jens Balke[a] ‡, Pierre Volz[a] ‡, Falko Neumann[b] ‡, Robert Brodwolf[a], Alexander Wolf[a], Hannah Pischon[c], Moritz Radbruch[c],Lars Mundhenk[c], Achim D. Gruber[c], Nan Ma[d], and Ulrike Alexiev[a]**

[a] Department of Physics, Freie Universität Berlin, Arnimalllee 14, 14195 Berlin, Germany.

[b] Institute of Chemistry and Biochemistry, Freie Universität Berlin, Takustraße 3, 14195 Berlin, Germany.

[c] Institute of Veterinary Pathology, Freie Universität Berlin, Robert-von-Ostertagstraße 15, 14163 Berlin, Germany

[d] Helmholtz-Zentrum Geesthacht (HZG), Institut für Biomaterialforschung Kantstr. 55, 14513 Teltow, Germany.

*corresponding authors: ulrike.alexiev@fu-berlin.de, nan.ma@hzg.de

KEYWORDS

time-resolved fluorescence spectroscopy, FLIM, reactive oxygen species, oxidative stress, reactive fluorescent dyes, nanotoxicity, live-cell imaging

ABSTRACT

Nanoparticles hold a great promise in biomedical science. However, due to their unique physical and chemical property, they can induce an elevated intra-cellular reactive oxygen species (ROS) production; consequently damaging DNA, proteins and lipids. Thus, there is a need for sensitive and reliable methods for intracellular ROS detection. We developed a fluorescence lifetime image microscopy (FLIM) based ROS detection approach (FLIM-ROX), which increases sensitivity and reliability of ROS detection in comparision with traditional methods. Using this method, we are able to distinguish autofluorescence from the unique fluorescence lifetime of the ROS reporter dye in its inactive and activated state in both living and fixed cells at the single cell level. At subtoxic concentrations of gold nanoparticles in macrophages, the oxidative stress was detected following nanoparticle uptake by FLIM-ROX, while being undetectable by the conventional method. Further, a statistical analysis approach was developed in order to process image data analysis in a high throughput manner. The versatility of FLIM-ROX was demonstrated by the detection of spatial ROS distribution in both healthy and atopic dermatitis model skin using multiphoton FLIM-ROX. This method allows cellular visualization and quantification of disease-induced oxidative stress levels in intact tissue, and thus can be used for monitoring the oxidative stress decline after treatment.

Adverse effect of nanoparticulate agents is a major concern in the advancing field of nanomedicine[1-2]. Currently, the molecular mechanism underlying cytotoxicity and genotoxicity of nanoparticles is not really understood. An important reason of nanotoxicity is the generation of reactive oxygen species (ROS). In ambient environment small quantities of reactive oxygen species (ROS), such as superoxide $O_2^{\bullet-}$, hydrogen peroxide H_2O_2, and hydroxyl radical $OH^{\bullet}$, are part of cell signaling and homeostasis regulation[3]. Low levels of ROS are produced by the respiratory chain and excess ROS can be reduced by antioxidant cellular defenses like catalase and superoxide dismutase to hydrogen and oxygen[4]. Overproduction of ROS, among others, is indicative of cellular stress that occurs under various environmental and disease conditions, *e.g.* upon nanoparticle uptake, in host defense against pathogens, as well as in cancer, atherosclerosis, diabetes, inflammatory diseases, and neurodegenerative disorders[2, 5-7]. Because of their highly reactive nature, elevated ROS levels can damage DNA, proteins, and lipids, thereby impairing normal cellular function.

Quantification of cellular ROS generation can be achieved by a variety of methods[8-9]. Reactive fluorescent dyes have emerged as a frequently used tool in quantifying ROS. As this topic has attracted a reasonable amount of attention, several dyes and methods have been established, most commonly using ELISA (plate reader) and flow cytometry approaches[8, 10-11]. Traditional dyes are dichlorodihydrofluorescein (DCF) and dihydroethidium (DHE) although there is a vast number of other dyes, each having their specific advantages, properties and applications. More importantly, there is a lack of coherent data in the literature for detecting different ROS *in vivo*[8, 12]. Among others, reliable detection of ROS is hampered by signal artefacts, such as in the case of DCF where besides oxidation of H_2DCF to the highly fluorescent DCF by ROS also other fluorescent products can be generated in the presence of high dye concentrations or at high light intensities[8]. In addition,

detection schemes, such as plate readers may detect fluorescence emission not only from the cells but also from the medium[8], as they do not discriminate single cells. Thus, these and other instrumental factors limit an accurate quantification of ROS. Moreover, intensity-based probes measure changes in the emission intensity of a single fluorescence peak and the results may be affected by variations in probe concentration and probe environment (in particular by pH or transition metals for the case at hand).

To overcome these and further obstacles, such as unreacted dyes and cellular autofluorescence, we employ the environmental sensitivity of the fluorescence lifetime in fluorescence lifetime imaging microscopy (FLIM)[13], a sophisticated technique that allows us to distinguish target fluorescence, in our case the ROS-activated dye fluorescence, from autofluorescence or unreacted dyes with single cell resolution. Moreover, fluorescence lifetime is independent of concentration and inner filter effects, thereby providing a very reliable method to localize and discriminate the ROS-activated fluorescent dye within the cell.

FLIM is often used to detect the cellular oxidative state through the measurement of NADH in its free and bound form reflecting the intracellular redox ratio[14-18], but to our best knowledge, FLIM has never used before to increase sensitivity and reliability of ROS detection using commercially available dyes.

Here, we demonstrate for the first time the applicability of our FLIM-based ROS detection method (FLIM-ROX). Using FLIM-ROX, we showed for paraformaldehyde fixed macrophages as well as in live-cell imaging of HeLa cells (i) a reproducible detection of intracellular free radical production through identification of the activated CellROX Green fluorescence lifetime signature in a highly precise manner, and (ii) a reproducible dependence of activated CellROX Green

intensity on H_2O_2 as well as on menadione concentration; the latter, as a naphthoquinone, undergoes intracellular redox cycling to produce $O_2^{\bullet -}$ [19].

Simulation of the binding of activated CellROX Green to DNA provides calibration curves that are sensitive in the low concentration range of the oxidative stressor and were used to quantify oxidative stress induced by gold nanoparticle uptake in macrophages. A high-throughput quantification of hundreds to thousands of single cells yielded similar results. We demonstrated the subsequent cellular adverse effect of low ROS levels by measuring morphological and cytoskeleton (F-actin) changes, elevated senescence, and DNA damage in macrophages after gold nanoparticle application. We also demonstrated the use of the FLIM-ROX method for detecting disease-induced enhanced ROS levels in skin biopsies from a murine atopic dermatitis model, paving the way to study and monitor enhanced ROS tissue levels, a potential trigger for controlled released of drugs from nanocarriers[20-21].

RESULTS AND DISCUSSION

Spectroscopic characterization and FLIM-ROX method development

CellROX Green operates in a two-step reaction, where the dye is first oxidized by ROS and after activation binds to double-stranded deoxyribonucleic acid (dsDNA), becoming highly fluorescent in the second step. Figure 1 A, B shows the molecular characterization of activated CellROX Green when bound to dsDNA in solution in terms of excitation and emission spectra, and the fluorescence decay curves. The fluorescence lifetime of dsDNA-bound CellROX Green as determined from the fluorescence decay in Figure 1B is bi-exponential with 4 ns (96 % amplitude) and 0.1 ns (4 %

amplitude). The short lifetime component may be attributed to the reporter dye still in the fluorescence quenched and reduced state.

The fluorescence lifetime curves were measured using time-correlated single photon counting (TCSPC)[22], a technique that requires low excitation intensities. Therefore, we used a TCSPC-based FLIM approach to study ROS within the cells[23]. FLIM image data analysis was facilitated by our cluster-based FLIM analysis tool that enhances image contrast due to the retrieval of fluorescence lifetime information with unprecedented accuracy and without the need to fit the individual lifetime curves pixelwise[13]. A white-light supercontinuum laser system provides multicolor picosecond excitation[13], allowing multiplexing for detecting different fluorophores such as CellROX Green (λ_{ex} =488nm), DAPI (λ_{ex} =405nm), CellMask Deep Red (λ_{ex} =640nm), or Cy5.5-labeled gold particles (λ_{ex} =640nm).

To develop the FLIM-based detection scheme of ROS we used the mouse macrophage cell line J774A.1. External cell stress was induced by high concentrations of H_2O_2 (0.15%) before fixation of the cells. Firstly, we compared the fluorescence localization of treated cells (Figure 1E) with autofluorescence in control cells (Figure 1I,J). The reliable localization of the activated DNA-bound CellROX Green by its lifetime signature is a prerequisite for further quantitative ROS studies. As shown by the magenta and red colored fluorescence decay curves of autofluorescence and activated CellROX Green, respectively, in Figure 1C, the fluorescence lifetimes of autofluorescence and activated CellROX Green clearly differed and can be discriminated by the cluster-based analysis algorithm[13]. Moreover, the average autofluorescence intensity was generally low with about 15 counts and autofluorescence primarily occurred in the cytoplasm of the macrophages (Figure 1 I-K). In contrast, Figure 1E and F shows the fluorescence lifetime based localization of activated CellROX Green in the nucleus of cells. The nuclear localization of

activated CellROX Green is confirmed using the DNA-stain DAPI (Figure 1F and G). CellMask Deep Red provides the outline of the macrophage cell morphology (Figure 1 G). The fluorescence lifetime decay curves of the two dyes DAPI and CellMask are different from activated CellROX Green bound to DNA and clearly separated from the cellular autofluorescence background fluorescence lifetime (Figure 1C), thus allowing multiplexing[24].

FLIM-ROX in live-cell experiments

We next tested the application of the FLIM-ROX approach in live cell experiments. As CellROX Green was shown to be sensitive to H_2O_2 in macrophages (Figure 1) we went now a step further and compared the sensitivity of CellROX Green to the two different exogeneous stressors H_2O_2 and menadione, the latter resulting in intracellular $O_2^{\bullet-}$ generation. Thus, living HeLa cells were investigated using increasing concentrations of H_2O_2 and menadione to establish a ROS concentration dependence of the activated CellROX Green signal.

The recorded fluorescence intensity images and the corresponding FLIM images of three different H_2O_2 concentrations (0%, 0.01%, and 0.1% H_2O_2) applied externally are presented in Figure 2. The intensity based images in Figure 2A, C and E indicate an intensity increase as function of increasing H_2O_2 concentrations. Moreover, using the additional fluorescence lifetime information obtained from FLIM, different populations of CellROX Green can be separated inside of the cell after discrimination from the background fluorescence (Figure 2B, D, F). The green and red colored areas correspond to different fluorescence decays of CellROX Green as obtained from the cluster-based FLIM analysis, with red being the fluorescence lifetime curve of CellROX Green bound to DNA in the nucleus and green the fluorescence lifetime curve of CellROX Green in the cytoplasm (Figure 2G). The basal value of cellular ROS species at 0% H_2O_2 is shown by the weak

activation of CellROX Green (Figure 2B), indicated by the red colored areas corresponding to activated CellROX Green bound to DNA in the nucleus.

The weak intensities of CellROX Green that we found in the cytoplasm (Figure 2D and F, green colored area) probably represent non-activated or only partially activated dyes as indicated by the appearance of an additional fast fluorescence decay component (Figure 2G, green curve) compared to the fully activated CellROX Green in the nucleus (Figure 2G, red curve). The fluorescence intensity of the CellROX Green lifetime cluster in the nucleus (red colored) is far higher than the green colored fluorescence lifetime cluster in the cytoplasm (Figure 2C-F). Moreover, a continuous intensity increase of the activated CellROX Green FLIM cluster in the nucleus in correlation to the different amounts of the extracellular stressor H_2O_2 was observed (Figure 2H), indicating a concentration dependent sensitivity of CellROX Green to H_2O_2.

A mathematical description of the CellROX Green FLIM intensity as a function of the activator concentration (*i.e.*, the stressor H_2O_2) was established using a Michaelis-Menten-like equation (eq. 2)[25]. Due to the fact that the ROS-activated CellROX Green to become highly fluorescent must bind to DNA, a saturation curve with increasing stressor concentration is expected and indeed seen in Figure 2I. The half-maximum stressor concentration is 0.016 ± 0.006 % externally applied H_2O_2. The highest sensitivity is in the low stressor concentration range, where the Michaelis-Menten-like curve appears to be linear. Using this linear relation in the lower H_2O_2 concentration range we obtain an upper estimate for the basal H_2O_2 level in the HeLa cancer cell line between 50 and 270 µM H_2O_2, although the real value might be much lower. Nevertheless, the clear-cut discrimination and detection of the lifetime signature from the activated DNA-bound CellROX Green serves as a highly sensitive read-out for ROS present in HeLa cells. Elevated values of internal H_2O_2

concentrations are known for cancer cells in contrast to healthy cells. In Jurkat cells, another cancer cell line, internal H_2O_2 concentrations of about 7 μM were reported[26].

Bearing the contradictory reported selectivities of CellROX Green for different ROS in mind[27-28] we further tested the sensitivity of CellROX Green towards menadione. In our live-cell FLIM studies with HeLa cells we observed similar concentration dependent effects for H_2O_2 and menadione. Figure 2J shows the respective calibration curve with a half-maximum stressor concentration of 9 ± 2 μM menadione. Thus, our FLIM-ROX results show that in human cells such as macrophages and HeLa cells the ROS reporter dye CellROX Green is sensitive to both H_2O_2 and superoxide in a quantitative fashion.

FLIM-ROX measurements of cellular stress induced by gold nanoparticles

As an application of FLIM-ROX in nanotoxicity we explored the possibility of detection on the nanoparticle induced cellular stress response in macrophages. We used cationic gold nanoparticles (AuNP) as a model system as there is very limited information for this type of metal-based nanoparticles on cellular stress[29].

First, we established a calibration curve with H_2O_2. Cells of the macrophage cell line J774A.1 were incubated with five different concentrations of hydrogen peroxide (0.01%, 0.025%, 0.15%, 0.3% and 0.6%) acting as an externally applied cellular stressor. The obtained FLIM images with their corresponding bright field images are shown in Figure 3A. The time-resolved fluorescence decays of CellROX Green in the cells show a homogeneous distribution with similar fluorescence lifetimes inside the nucleus. Therefore, the intensity profiles of cells are recorded and the mean intensities are calculated using 6 cells for each H_2O_2 concentration. The background-corrected maximum intensity in the saturation limit of I_{max}= 1230 ± 50 counts can be deduced from the

calibration curve and the Michaelis-Menten-like fit (eq. 2) in Figure 3F. Maximum CellROX Green intensity is thus far above the avarage autofluorescence with about 15 counts as determined from control cells (Figure 1K). The concentration of H_2O_2 to reach half saturation is $c_{1/2}$= 0.17 ± 0.07 %. Here, in fixed macrophages the half saturation value for H_2O_2 is slightly higher than for live HeLa cells (Figure 2I) indicating a cell type dependence.

Next, we used this calibration to investigate the level of oxidative stress in macrophages after application of AuNP in a subtoxic dosage according to previous studies[1]. Cell viability measurements indicated that the 25 nm AuNP are non-toxic to macrophages at 10 µg/ml (Figure 4E), having a relative cell viability of 96 % and not showing a significant difference compared to the untreated control cells.

Figure 3 B and C shows the distribution of the AuNPs inside and outside of the cells after one hour of incubation as bright field and FLIM image using the fluorescence of the Cy5 dye attached to the nanoparticle surface. In the bright field image (Figure 3B) AuNPs outside of the cells appear as black small clusters and are barely visible in the FLIM image probably due to clustering-induced quenching. In the cytoplasm, the nanoparticles are almost homogeneously distributed (Figure 3C). Flow cytometry experiments (Figure 3D) demonstrated similar uptake behavior. As these measurements indicate, the entire cell population shows a higher mean fluorescence intensity compared to the untreated cells after one hour exposure, with a fairly even distribution of the gold nanoparticles in the complete cell population.

From the intensity-based FLIM-ROX image in Figure 3E an average value of the activated DNA-bound CellROX Green signal was obtained from 6 individual cells. The calibration curve in Figure 3F was then used to obtain the oxidative stress level induced by the gold nanoparticles. A

value comparable to 0.06 ± 0.01 % H_2O_2 was determined, which is below the half-maximal concentration of the calibration curve, *i.e.* in the lower linear range.

Comparison of AuNP induced cellular stress and biological adverse effects

Although the AuNP did not show cytotoxicity in the cell viability test, we observed a cellular stress response upon uptake. To be sure that cytotoxicity was negligible, further tests were performed (Figure 4E). All tested concentrations were not toxic to these cells as even the highest concentration was about 80 % of cell viability.

Next, we studied biological adverse effects such as actin stress fiber formation, senescence induction and DNA damage that may result from the subtoxic cellular oxidative stress response. The gold nanoparticles had a visual effect on the actin stress fiber F-actin formation indicating a change in cell movement proteins after 24 hours (Figure 4A-D). The particles themselves are accumulated in the perinuclear area. Confocal laser scanning microscopy pictures have been taken using J774A.1 and primary human macrophages for imaging. Note the formation of spikey and compact actin structures upon AuNP internalization compared to the untreated control cells (Figure 4 A and C *vs* B and D).

Similar to the F-actin results, cellular senescence as demonstrated by the increased ß-galactase activity (Figure 4F) as well as DNA damage detected by the Comet assay (Figure 4G) were increased in macrophages upon AuNP treatment.

These finding together indicate slight irritations of cellular homeostasis both in mouse and in human donor cells suggesting a higher impact for the evaluation of nanoparticles at low concentrations when applied in nanomedicine.

A statistical FLIM-ROX assay for high-throughput applications

For high-throughput applications, it is desirable to establish a quantitative assay for investigating the cell stress of 100s to 1000s of cell at the same time. Here, we also extended the single cell FLIM-ROX assay to these type of applications without sacrificing the single cell information. This was realized using FLIM-ROX with a 4x objective. The measured field of view had a side length of 1.5 mm, allowing to record about 500 cells per single measurement in the given setup. The recorded fluorescence intensity and cluster-based FLIM-ROX images are presented in Figure 5.

In order to analyze the fluorescence intensity of an individual cell, it must first be localized. The cells were identified by the center of the fluorescence intensity from the point spread function (Figure 5A and B). To obtain the activated CellROX-Green intensities of the individual cells (Figure 5C), a proper gaussian preprocessing threshold was applied. Then, a particle detection was performed using a generalized likelihood ratio test. After obtaining the coordinates for each intensity maximum of the cells, the intensity in a circle with the maximum in its center was integrated. A doughnut shaped area around this circle (yellow) was used to exclude background noise (Figure 5 C). The size of the first circle was chosen with a diameter of 3 µm to include all the fluorescence intensity from the nuclei. The doughnut had an outer diameter of 5µm. The method is schematically shown for two H_2O_2 concentrations using a single fluorescence intensity images of a selected cells as 3D image (Figure 5C). The integrated intensities for a given stressor concentration were evaluated from the respective histograms using Gauss fitting as shown in Figure 5D with three different H_2O_2 concentrations. The corresponding calibration curve is presented in Figure 5E. A maximum intensity I_{max}= 2200 ± 200 counts and half saturation $c_{1/2}$= 0.12 ± 0.04 % H_2O_2 was obtained from the fit with the Michaelis-Menten-like equation (eq.2). This curve is almost similar to the calibration curve obtained from the single cell measurements

shown in Figure 3F. The integrated FLIM-ROX intensity of the AuNP exposed cells is marked (Figure 5E) and yields a similar result compared to the single cell measurements (0.06 ± 0.01 % H_2O_2 (Figure 3F)) with a value of 0.07 ± 0.02 % H_2O_2 , thus also validating the statistical single cell based approach for high-throughput analysis.

Application of multiphoton FLIM-ROX to living tissue

The application of FLIM-ROX is not limited to cellular studies. As a further application of FLIM-ROX, we quantified the ROS production in whole skin tissue, in particular in the stratum corneum of diseased skin. The stratum corneum, the outermost layer of skin, may be altered in several skin disease conditions like atopic dermatitis (AD). The stratum corneum consist of corneocytes, terminally differentiated keratinocytes that are metabolically inactive. Corneocytes are embedded in a lipid matrix consisting mainly of ceramides, free fatty acids and cholesterol. Typical corneocyte structures can be seen in the confocal image in Figure 6A.

It is known that oxidative stress promotes inflammatory diseases of the skin as in the case of AD[7]. Moreover, inflammatory cells release free radicals when activated, increasing the effect of oxidative stress[7]. For testing oxidative stress in diseased skin we chose a murine animal model of AD and quantified the ROS level in the stratum corneum. Figure 6 shows representative FLIM-ROX images of CellROX Green treated skin biopsies of healthy murine skin (Figure 6C), UVB irradiated murine skin (Figure 6B) serving as negative and positive control for the AD model (Figure 6D), respectively. Red colored pixels are indicative for regions of high ROS levels. Pixel of other colors are inactivated CellROX Green or autofluorescence as determined from the cluster-based FLIM analysis and the respective fluorescence lifetime signature. Within the negative control, red areas are limited to a few small cell compartments, the positive control is characterized

predominantly by red areas, indicating increased oxidative stress due to extensive UVB irradiation [30]. We further quantified ROS by cluster-based FLIM analysis using the corrected mean fluorescence intensity of CellROX Green in the FLIM-ROX assay (Figure 6E). In healthy murine skin, the addition of CellROX Green ("+CellROX", without activation) increases the fluorescence intensity by 36% with respect to the autofluorescence background ("-CellROX"). Activation with UVB radiation (50 mJ/cm²) induces oxidative stress and yields a fluorescence increase of 263%. While in AD murine skin autofluorescence background is reduced to a fraction (15%) of healthy murine skin, the intensity immediately increases after addition of CellROX Green to 3560% over baseline level, indicating significant ROS levels in the AD model skin compared to healthy murine skin. Our multiphoton FLIM-ROX approach outperformed previously reported methods which are solely intensity based[30] by means of spatial resolution, selectivity and signal artefact reduction. This allows for the precise assesment and monitoring of enhanced ROS levels in tissue. Enhanced ROS levels can be utilized as triggers for controlled release of drugs from nanocarriers, thus the FLIM-ROX data might prove useful in drug delivery.

CONCLUSION

Our studies demonstrate that a FLIM-based analysis of the CellROX Green signal to detect ROS provides reliable and reproducible quantification of ROS generation in human cells upon nanoparticle treatment and disease-induced ROS levels in inflamed murine skin using FLIM-ROX. The combination of TCSPC-FLIM and our cluster-based analysis algorithm provides accurate fluorescence lifetime signatures of the activated DNA-bound CellROX Green dye both in living cells and tissue. These accurate assignments of the intracellular fluorescence to the activated ROS reporter is a prerequisite for quantitative ROS level analysis. Using this single cell based approach and CellROX Green as an examplary ROS reporter dye we showed that even lower levels of ROS

generation by nanoparticles in the subcytotoxic range can affect cellular homeostasis. We further demonstrate that CellROX Green selectivity for certain ROS may vary between different cell types. In our experiments, CellROX green was sensitive towards externally applied H_2O_2 and menadione generating superoxide. Our single cell based FLIM-ROX approach was extended to the analysis of many single cells in a statistical analysis making our FLIM-ROX technique also useful for high-throughput measurements. The half saturation value of the calibrations curves obtained from the single cell and from the statistical approach is the same within statistical uncertainty, thus validating the high-throughput assay. Consequently, it is possible to scan samples at a high rate with the benefit of high numbers of investigated cells using FLIM-ROX. Moreover, we demonstrated that the FLIM-ROX method is applicable to tissue measurements when combined with multiphoton excitation providing unprecedented imaging contrast through autofluorescence separation from CellROX Green fluorescence localization combined with ROS quantification.

Taken together our results underline the potential of fluorescence lifetime-based imaging for cellular and tissue studies of oxidative stress using our FLIM-ROX approach that in addition allows spectral multiplexing and molecular imaging. Applications are not limited to nanomaterial induced oxidative stressed as shown by the monitoring of disease-induced stress levels in whole tissue samples.

METHODS

Materials

CellROX® Green, dsDNA, L-glutamin, CellMask™ Deep Red, SYBR® Green I, Alexa Fluor™ 488 Phalloidin, RPMI, Glutamine, Calf-Serum, MCSF, SYBR Green, penicillin and streptomycin were purchased by ThermoFisher Scientific (USA). AuNP labeled with Cy5.5 NHS-Ester are from Nanopartz (US/Canada). PBS, H_2O_2, Menadione, NaOH, EDTA and DAPI were obtained by Sigma Aldrich (Germany). CellView-dishes are from Greiner bio-one (Germany) and Willco-dishes (GWSt-3522) from Willcowells (Netherlands). Fetal bovine serum (FBS) was purchased by Biochrom (Germany) and low-glucose Dulbecco's modified Eagle's medium (DMEM) by Lonza (Swiss). All other chemicals were of the highest purity available.

Steady state fluorescence spectroscopy

We measured fluorescence excitation and emission spectra with a Fluoromax-3 (Horiba Jobin Yvon, Japan) using 3×3 mm quartz cuvettes. The temperature was set to 20 °C. The excitation spectrum is recorded at λ_{em}=525 nm by changing the excition wavelength from λ_{ex}= 435 to 525 nm in 1 nm steps. For the emission spectrum the sample was excited at λ_{ex}=480 nm and the fluorescence emission was recorded between λ_{em}=500 and 750 nm with a spectral resolution of 1 nm. We activated CellROX Green by adding 15% H_2O_2 and 50 ng/ml dsDNA (salmon testiculis) for 30 minutes.

Time-resolved fluorescence spectroscopy

We performed time-resolved fluorescence spectroscopy in a home-built time correlated single photon counting (TCSPC) based cuvette apparatus as described previously[31-32]. CellROX Green

fluorescence was excited by a picosecond frequency-doubled diode-pumped Nd:YVO_4 mode-locked titan:sapphire-laser (Millenia Vs, Tsunami, Frequency Doubler #3985, Spectra Physics, USA) at 488 nm. A pulse selector (Pulse Selector #3980, Spectra Physics, USA) reduced the laser repetition rate from 82 MHz to 4.05 MHz. The excitation power was adjusted to approximately 100-150 µW by neutral density filters. After passing a 515 nm long pass filter (OG 515, Schott, Germany), fluorescence photons were detected by a micro channel plate photomultiplier tube (MCP-PMT, model #R3809U, Hamamatsu, Japan). A TCSPC module (SPC-830, Becker & Hickl, Germany) sorted the detected fluorescence photons into histograms of 1024 time bins with a width of 19.7 ps. An instrument response function (IRF) was recorded using the scattering light of a colloidal silica solution "LUDOX" (Grace, USA) without long pass filter. The recorded IRFs were smaller than 40 ps full-width half-maximum (FWHM). We analyzed the recorded fluorescence decay curves by using the program Global Unlimited V2.2 (Laboratory for Fluorescence Dynamics, University of Illinois, USA). After the deconvolution of the fluorescence signal and the IRF, the time-dependent decay profile was fitted to a sum of exponentials $I(t)$ by an iterative non-linear least-squares analysis:

$$\mathrm{I(t)} = \sum_{\mathrm{i}}^{\mathrm{n}} \alpha_{\mathrm{i}} \mathrm{e}^{-\mathrm{t}/\tau_{\mathrm{i}}} \quad \text{(eq. 1)}$$

with n the total number of decay components; α_i the amplitude and τ_i the fluorescence lifetime of the ith component.

Fluorescence lifetime image microscopy (FLIM)

Time-resolved fluorescence imaging was conducted in a home-built fluorescence lifetime imaging microscopy (FLIM) setup which combines TCSPC and confocal laser scanning

microscopy (CLSM)[13, 33].A ps-pulsed super continuum laser source (NKT SuperK Extreme EXU-3, NKT Photonics, Denmark) generated a white light spectrum with a pulse repetition rate of 19.5 MHz. To excite CellROX Green exclusively, a narrow (3.6 nm) spectral band at 488 nm was cut out of the white light spectrum by an acousto-optical tunable filter (AOTF, UV-VIS Select, NKT Photonics, Denmark). The excitation laser beam was focused by an objective (4x air or 60x water, RMS4X or UPSLAPO60XW, Olympus, Japan) and scanned over the sample located on an inverted microscope (IX71, Olympus) by a DCS-120 scanning unit (Becker&Hickl, Germany). For live-cell applications, a temperature controlled specimen holder was installed and adjusted to 37°C. Fluorescence emission is selected by a band pass filter 525/50 nm (BrightLine HC, Semrock, USA) and detected by a hybrid PMT detector (HPM-100-40, Becker & Hickl, Germany). For co-localization of CellROX Green and Cy5.5-labelled gold nanoparticle (AuNP), we selected a spectral band at 640 nm (7 nm width) for C5.5 excitation, in addition to the 488 nm band and used a second detector. The fluorescence emission was spectrally separated using a dichroid mirror at 570 nm (Becker & Hickl, Germnay) and filtered by a 525/50 nm bandpass (BrightLine HC, Semrock, USA) and a second bandpass 708/80 nm (BrightLine HC, Semrock, USA) located in front of the second hybrid detector (HPM-100-40, Becker & Hickl, Germany). The instrument response function (IRF) of the setup has a FWHM of 120 ps. The collected photons are sorted into 1024 time channels with a bin width of 19.5 ps by a TCSPC module (SPC-160, Becker & Hickl, Germany). For co-localization of the fluorescence of CellROX Green, the cells additional stained with DAPI and CellMask Deep Red are excited at 640 nm and 405 nm respectively. To collect the fluorescence of DAPI a long pass filter 435 nm (BrightLine HC, Semrock, USA) and for CellMask Deep Red a long pass filter 665 nm (Chroma, USA) are used.

Raw FLIM data were analyzed using self-written routines in C++. Fluorescence decay traces of the individual pixels are partitioned into classes (*i.e.* clusters) using a multivariate pattern recognition method. False-color images are generated by assigning a distinct color to all pixels containing a fluorescence decay curve that belonged to a certain cluster (*e.g.* different fluorescence decay species of CellROX Green, indicating activation and autofluorescence of cells).

Multiphoton FLIM

Multiphoton FLIM was conducted in a home-built setup. For multiphoton excitation we used a mode-locked pulsed femtosecond titan:sapphire-laser (Mira 900, Coherent, USA). The titan:sapphire-laser was pumped by a continuous wave semiconductor laser (Verdi V5, Coherent, USA) at 532 nm. The titan:sapphire-laser system produces laser pulses shorter than 200 fs at 800 nm with a repetition rate of 76 MHz. An objective (60x water, UPSLAPO60XW, Olympus, Japan) focuses and a scanning unit (DCS-120, Becker & Hickl, Germany) scans the excitation laser beam over the sample placed on an inverted microscope (IX-73, Olympus, Japan). Fluorescence emission was separated from excitation light by a dichroic mirror (H 643 LPXR superflat, AHF, Germany) and a short pass filter (SP745 BrightLine HC, Semrock, USA). CellROX Green fluorescence was distinguished from the fluorescence of other fluorophores by a band pass filter (525/50 BrightLine HC, Semrock, USA). Fluorescence photons were collected in non-descanned detection (NDD) mode by a hybrid detector (HPM-100-40, B&H, Germany). The instrument response function (IRF) of the setup is 120 ps (FWHM). The collected photons are sorted into 1024 time channels with a bin width of 19.5 ps by a TCSPC module (SPC-150, Becker & Hickl, Germany). The same cluster-based FLIM analysis as for one photon FLIM was applied for multiphoton FLIM. FLIM images of UVB irradiated and non-irradiated murine skin samples after CellROX Green application were measured for 10 min. The mean FLIM-ROX intensities in Figure

6D are based on the intensities of pixels belonging to the red colored FLIM signature assigned to areas of activated CellROX Green.

FLIM-ROX method

CellROX® Green (ThermoFischer, USA) is a cell membrane permeable reagent. After oxidation CellROX Green shows a high binding affinity towards dsDNA, which leads to an enrichment of the reagent in the cell nucleus upon activation. The fluorescence excitation maximum of activated CellROX Green is located at λ_{ex} = 485 nm and the fluorescence emission maximum at λ_{em} = 520 nm. The stock solution of 2.5 mM CellROX Green was stabilized in dimethyl sulfoxide (DMSO) and diluted in phosphate buffer saline (PBS) at pH 7.4 to concentration of 5 µM. The diluted sample was stored in the dark at 4°C prior to all measurements.

Before fixated and living cells were investigated by FLIM, they were incubated with 5 µM CellROX Green at 37°C for 30 min in CellView dishes (Greiner bio-one). After incubation, we washed the cells three times with PBS and subsequently started FLIM measurements. A single FLIM image was recorded for 10 minutes. Raw FLIM data were analyzed by our cluster-based FLIM analysis (see above) and thereby activated CellROX Green was separated from inactive CellROX Green and autofluorescence. For the data analysis of our single cell assay we used the averaged peak intensities of up to 6 cells to determine calibration curves of cellular stress by H_2O_2 and menadione. For the calibration the concentration of H_2O_2 in the CellView dish was varied from 0.000003 % to 0.6 % and the concentration of menadione from 0 to 100 µM and measured the incubated cells by FLIM. After the FLIM analysis, we fitted the resulting concentration dependent CellROX Green intensities by a Michaelis-Menten-like equation[25]

$$I = I_{max} \frac{c_{activator}}{c_{1/2}+c_{activator}} \qquad \text{(eq. 2)}$$

with I_{max} being the maximal intensity, $c_{activator}$ the concentration of H_2O_2 or menadione and $c_{1/2}$ the half-maximum activator concentration. The calibration curves are used for the comparison of the cellular stress level of an investigated oxidative stress inducer with the reference oxidative stress-inducing agents H_2O_2 or menadione.

For the high throughput, *i.e.* the measurement of a large number of cells, the FLIM-ROX assay, the FLIM setup was used with a 4x objective (Olympus), thereby increasing the cell number in the field of view (FOV) to up to 500 cells per single FLIM measurement. All experimental conditions were the same as above except the measurement time, which was reduced to 180 s. Each cell in the FOV was localized and the intensity in the nucleus was integrated. To identify single cells in the ensemble, we used a general likelihood approach. This approach is part of the particle finding algorithm localizer (IgorPro, Wavemetrics, USA). After obtaining the coordinates for each intensity maximum of the cell nucleus, the intensity in a circle with the maximum in its center is integrated by a self-written Python program. The radius of 3 µm is chosen in accordance to the cellular intensity distribution. A doughnut shaped area (diameter 5 µm) around this circle excludes the background noise and ensure only the intensity of the nucleus is evaluated. The calculated integrated intensity of each cell is sorted in a histogram. The obtained statistical intensity distribution from about 500 cells per image shows a normal distribution for each concentration. The expectation values were obtained by Gaussian fitting of the distributions and used for quantification of the cellular stress. Again, calibration curves of H_2O_2 and menadione were recorded and subsequently fitted with equation 2.

FLIM-ROX with live-cell FLIM of HeLa cells

HeLa cells were obtained (#ACC57, Leibnitz Institute DSMZ - German Collection of Microorganisms and Cell Cultures) and were cultivated in RPMI 1640 medium with L-glutamin (supplemented with 10% (v/v) fetal bovine serum (FBS) Superior, Biochrom), 1% non-essential amino acids and 1% penicillin/streptomycin at 37 °C and 5% CO_2. Prior to experiments, HeLa cells were seeded in CellView-dishes (Greiner bio-one) at a concentration of 10^6 per sample. On the same day the samples were incubated in PBS with different H_2O_2 concentrations for one hour at 37° C and 5% Co_2. The medium was exchanged with PBS and 5 µM CellROX Green and incubated for 30 minutes. After incubation the cells were washed with PBS and measured using the described FLIM-ROX method.

Cell culture of mouse macrophages and human macrophages

Macrophage mouse cell line J774A.1 cells (Sigma Aldrich, Germany) were grown in low-glucose Dulbecco's modified Eagle's medium (DMEM, Lonza) supplemented with 10 % fetal bovine serum (FBS), 1% glutamine and 1 % streptomycin. For cultivation the cells were kept at 37° C and an atmosphere with 5 % CO_2.

Primary human macrophages were generated from peripheral blood mononuclear cells (PBMCs), isolated from the buffy-coats (NycoPrep 1.077) of anonymous healthy volunteers with permission (Deutsches Rotes Kreuz, Berlin, Germany). After three washing steps using Ca^{2+}/Mg^{2+} free phosphate buffered saline (2 mM EDTA), monocytes were separated from the PBMCs using $CD14^+$ MicroBeads (clone HI149; Miltenyi Biotech) and magnetic cell separation according to the manufacturer's instructions. Subsequently, monocytes were cultured in complete growth media (RPMI-1640 supplemented with 2 mM L-glutamine, 100 U/ml penicillin, 100 mg/ml streptomycin

10% heat-inactivated fetal calf serum and 20 ng/ml MCSF). After six days, mature macrophages were obtained as confirmed by the expression of the cell surface markers CD11b, CD14, CD206 and absence of CD1a (flow cytometric analysis, FACSCalibur, (Becton Dickinson, Heidelberg, Germany). For the Cytoskeleton studies, the cells were also stained with Atto-Phalloidin 594 (160 mM) and DAPI (25 ng/ml) for 30 minutes. Imaging for this study was performed on a CLSM (Leica SP8, Germany) and analyzed by Leica Application Suite X software.

Preparation of fixed Macrophage cells with CellROX Green and AuNP for FLIM-ROX

774A.1 cells were seeded in 35 mm glass bottom CellView-dishes (Greiner Bio One) with a density of $1 \cdot 10^5$ cells per compartment. After 24 hours the cells were exposed to the desired H_2O_2 concentration for 30 minutes. 10 µM CellRox® Green in PBS was used to replace the cell medium for 30 minutes. Cells were then washed with PBS and fixed in 4% paraformaldehyde for 20 minutes. Cells were mounted with Pro Taqs® Mount Fluor (Biocyc, Luckenwalde, Germany) and kept at 4°C in the dark until the measurements were conducted. For further localization of the fluorescence collected, the cells are stained with 2.5 µg/ml DAPI and 2.5 µg/ml CellMask Deep Red and cells were peameabilised with 0.1% Triton(TM) X-100 for 5 minutes.

For gold nanoparticles (AuNP) induced ROS quantification J774A.1 cells were treated with 10 µg/ml of gold nanoparticles for 1 hour in DMEM prior to washing with PBS. Spherical gold nanoparticles (diameter 25 nm) enveloped by an amine coating and covalently bound Cy5.5 NHS-Ester (Lumiprobe, USA) with an absorption maximum at λ_{ex} = 673 nm an emission at λ_{em} = 707 nm have been purchased by Nanopartz (Loveland, US/Canada). A concentration of 10 µM CellRox Green in PBS was used to replace the cell medium for another 30 minutes. Cells were then washed and fixed in 4% paraformaldehyde for 20 minutes. Cells were mounted with Pro

Taqs® Mount Fluor and kept at 4°C in the dark until the measurements were conducted. The FLIM images based on the distribution of fluorescence lifetimes of CellROX Green in macrophages (cell line J77AA.1, fixated) stressed by different extracellular concentrations of H_2O_2 (0.015%, 0.025%, 0.15%, 0.3% and 0.6%) and spherical AuNP were analyzed using the FLIM-ROX method.

Gold particle uptake experiments and cellular effects

25.000 J774A.1 cells per well in a 24 well plate were treated with 10 µg/ml of gold nanoparticles for 1 hour in DMEM prior to washing with PBS. Washed cells were scraped off and centrifuged 4 minutes at 140 g. The pellet was resuspended in 100 µl PBS and kept on ice until measurement in a BD Accuri™ C6 flow cytometer (Becton Dickinson, Heidelberg, Germany). The mean fluorescence intensity of three independent experiments was then averaged. The data was analyzed using the FlowJo® 10 software (LLC).

For the cell viability measurements using the CCK-8 test the macrophages were incubated for 24 hours with three different nanoparticle concentrations ranging from 1, 10 and 50 µg/ml in three independent experiments. As a cutoff value, the ISO 10993-5-2009 standard value of 70 % relative cell viability was used to differentiate toxic and non-toxic concentrations. 1 % of SDS as a positive control was used to validate the assay.

For the cytoskeleton studies, the cells were stained with Alexa Fluor™ 594 Phalloidin and DAPI for 30 minutes. Imaging for this study was performed on a cLSM (Leica SP8, Germany) and analyzed by Leica Application Suite X software.

For SA-β-galactosidase activity assay the J774A.1 cells were seeded in a 96-well plate at a density of 2.000 cells per well and allowed to attach overnight. Gold nanoparticles and doxorubicin

as a positive control were applied to fresh cell culture medium at concentrations of 10 µg/ml and 500 nM, respectively. The assay was performed according to the manual of the assay kit CBA-231 (Cell Biolabs, USA). In short, cells were washed, lysed and the lysate was treated with x-gal. Fluorescence was measured at 360 nm/465 nm. The incubation times for this test were 24 hours and 48 hours.

The alkaline comet assay was performed according to the Trevigen Single Cell Gel Electrophoresis Assay protocol (Trevigen®, Gaithersburg, USA), by seeding 5×10^4 cells/well in a 24 well plate. After attachment overnight, the cells were exposed to gold nanoparticles. After 24 hours, the cells were harvested, washed with PBS and resuspended with preheated (37 °C) 1% low-melting agarose. The solution was spread over a glass slide and allowed to solidify for 15 minutes. Afterwards, cells were lysed for one hour at 4 °C using the kits lysis buffer. The slides were then immersed in a gel electrophoresis tank containing cold electrophoresis buffer (200 mM NaOH, 1 mM Na_2EDTA, pH = 13) for one hour at 4 °C in the dark. Electrophoresis was conducted for 60 min at 4 °C, 300 mA and 0.96 V/cm. The slides were washed twice with deionized water, once with 70 % ethanol and air-dried at 37 °C for 15 min. The DNA was stained using SYBR® Green I Nucleic Acid Stain at a 1:10.000 dilution. At least 100 cells per slide and 3 slides per treatment were examined using an AxioVert1 fluorescence microscope (Zeiss, Jena, Germany) and Zen software (Zeiss). DNA damage was expressed as the tail moment.

Sample preparation and measurement condition for multiphoton FLIM-ROX

Ex vivo murine skin was originated from an experiment approved by the State Office of Health and Social Affairs, Berlin, Germany (LaGeSo; G 0038/15). The AD model was induced via repeated topical hapten applications with oxazolone (OX, Sigma-Aldrich, USA) in six- to eight-

weeks-old, male, hairless SKH-1 mice (Charles River, Germany) as described before[34] with minor modifications. Briefly, mice were sensitized (day 0) with 5% oxazolone on a 3 cm x 1.5 cm area only of the right flank, followed by five repeated challenges every other day starting one week after sensitization (days 7, 9, 11, 13 and 15) with 0.1% OX. The healthy contralateral flank remained untreated.

Immediately after sacrification of the mice on day 17 tissues of the inflamed (AD model) right and the contralateral healthy flanks were collected as punch biopsies with a diameter of 8 mm. The skin was then placed on cell culture insets for 12 well plates (0.4 µm pore size, Corning, USA), humidified and left at room temperature for approximately two hours. Subsequently, the tissue samples were suspended in 500 ml DMEM-F12/DMEM-Glutamaxx (containing: 50 ml fetal bovine serum, 5 ml penicillin/streptomycin and phenolred) and placed in an incubator at 37°C (CO_2=5%).

For multiphoton FLIM-ROX (mpFLIM-ROX) assay, skin samples were cut with the cell culture inset laid top down onto a Willco-dish (GWSt-3522, Willcowells) and humidified by filter paper soaked with PBS. For incubation with CellROX Green, the sample was incubated in 500 µl PBS (100 µM CellROX Green) for 15 minutes. Before measuring by mpFLIM, the sample was rinsed with PBS. Positive control samples were UVB-irradiated in a UVB chamber (BIO-LINK crosslinker, Vilber Lourmat) with a dose of 50 mJ/cm^2 at 312 nm using five 8W lamps (BLX-312, Vilber Lourmat).

FIGURES

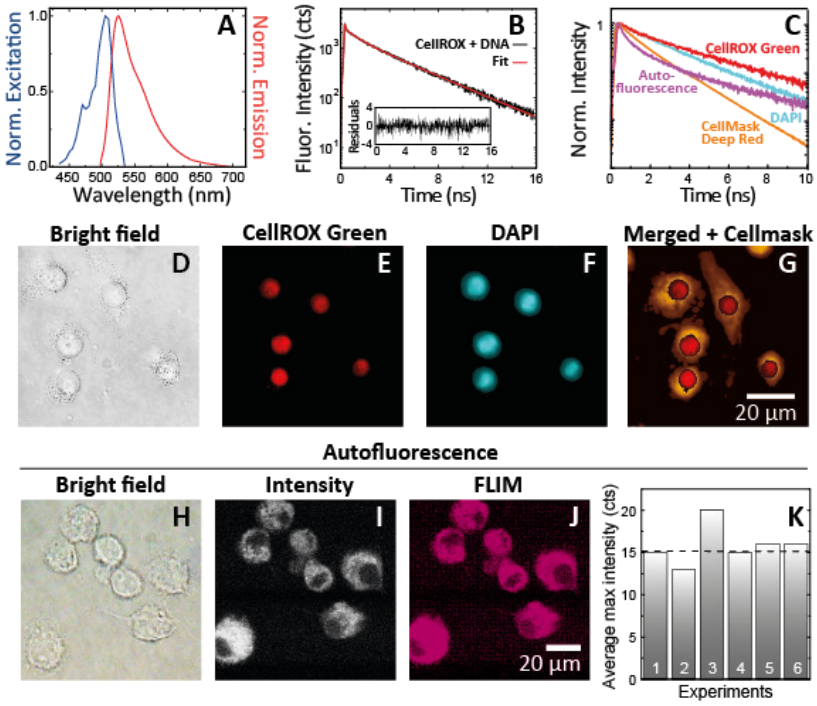

Figure 1. Characterization and cellular localization of activated (*i.e.*, oxidated) CellROX Green bound to dsDNA. (**A**) Normalized excitation and emission spectra. (**B**) Fluorescence decay curve of oxidated CellROX Green bound to dsDNA in solution. (**C**) Fluorescence decay curves with color coding according to the FLIM images of J77AA.1 cells shown (**E-G**) and **(J**). (**D-G**) Bright field image and FLIM images of (**E**) CellROX Green, (**F**) DAPI, and merged FLIM image of DAPI and CellROX Green with additional CellMask Deep Red staining (**G**). (**H-J**) Autofluorescence characterization of fixed J77AA.1 cells as shown as (**H**) bright field image, (**I**) intensity image, and (**J**) FLIM image. (**K**) Average maximal autofluorescence intensities in J77AA.1 cells.

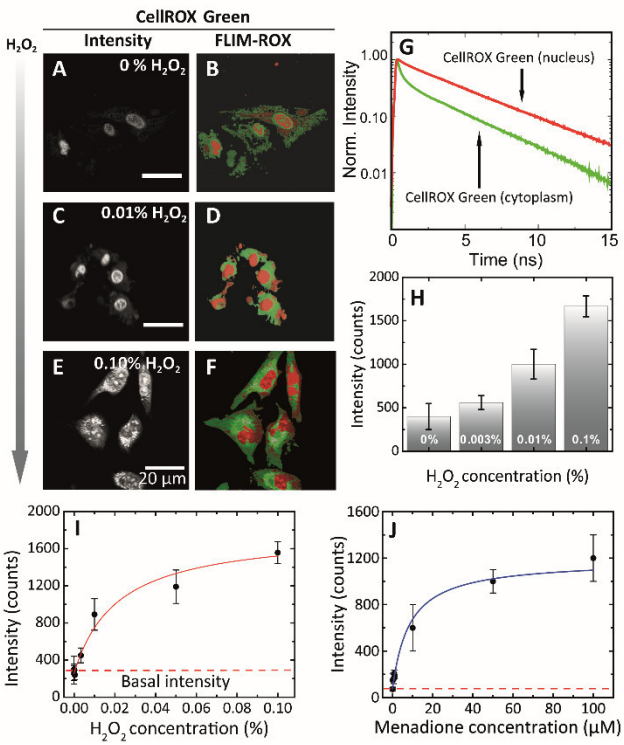

Figure 2. Live-cell FLIM-ROX measurements using HeLa cells show a difference in CellROX Green lifetime between nucleus and cytoplasm. (**A-F**) Intensity and FLIM-ROX images at different H_2O_2 concentrations. False color coding of FLIM-clusters in (**B**, **D** and **F**) according to the different fluorescence lifetime signatures of CellROX Green in the cytoplasm and the nucleus as shown in (**G**). (**H**) CellROX Green intensity inside the cell nucleus at varying H_2O_2 concentrations. (**I**) H_2O_2 calibration curve and (**J**) menadione calibration curve of the FLIM-ROX signal with a Michaelis-Menten-like fit curve (eq. 2).

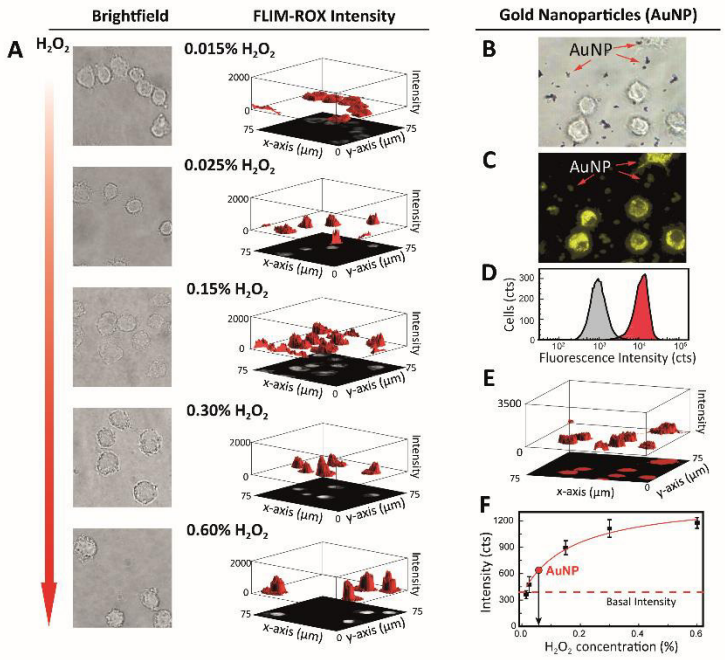

Figure 3. Single cell FLIM-ROX measurements of gold nanoparticle (AuNP) stress response in macrophages. AuNP diameter: 25 nm. (**A**) Bright field and CellROX Green FLIM intensity images of fixated J77AA.1 cells. Images of J77AA.1 cells with Cy5.5 labeled-AuNP as (**B**) bright field, (**C**) Cy5.5 FLIM image. (**D**) Results from flow cytometry measurements. (**E**) FLIM-ROX intensity image. (**F**) H_2O_2 calibration curve of the CellROX Green FLIM-ROX signal with a Michaelis-Menten-like fit curve (eq. 2). The FLIM-ROX signal intensity of AuNP induced ROS is marked with an arrow.

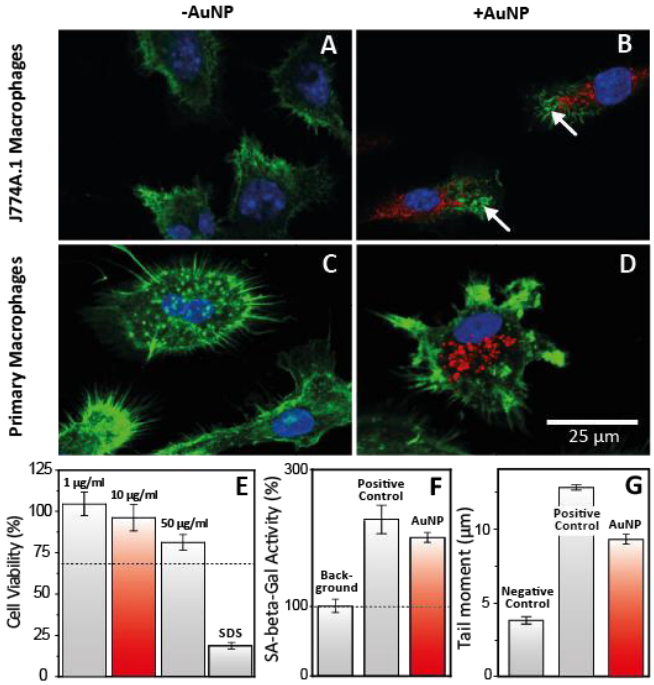

Figure 4. Adverse effects of gold nanoparticles (AuNP) at subcytotoxic concentrations. (**A**) and (**C**) F-Actin staining in untreated J774A.1 cells and primary human macrophages, respectively. (**B**) and (**D**) cells treated with AuNP, the arrows point towards F-actin condensation. (**E**) Cell viability measurement using CCK-8. (**F**) Senescence-associated β-Gal activity measurement. (**G**) Comet assay for the detection of DNA damage. All tests were performed after 24 hours.

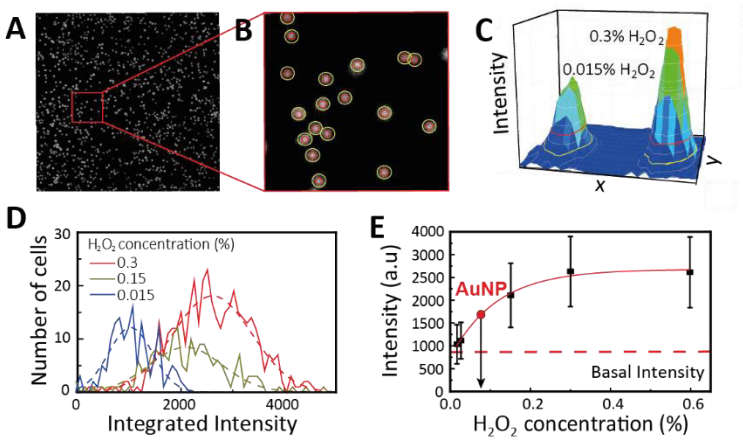

Figure 5. Statistical FLIM-ROX approach for high-through put and fast evaluation of a high number of cells. *(***A**) Using a lower magnification with a field of view diameter of 1.5 mm. (**B**) Single cells are identified. (**C**) 3D schematic of the red and yellow circle used to discriminate the activated CellROX Green signal against background. Yellow circle for background exclusion. Red circle for inclusion of fluorescence intensity from CellROX Green in the nucleus. (**D**) The obtained and binned integrated single cell CellROX Green intensities are shown together with a Gaussian fit for three H_2O_2 concentrations. (**E**) The expectation values from the Gauss fit in (**D**) are plotted as a function of the stressor concentration yielding the calibration curve with a Michaelis-Menten-like fit curve (eq. 2). The FLIM-ROX signal intensity of AuNP induced ROS is marked with an arrow.

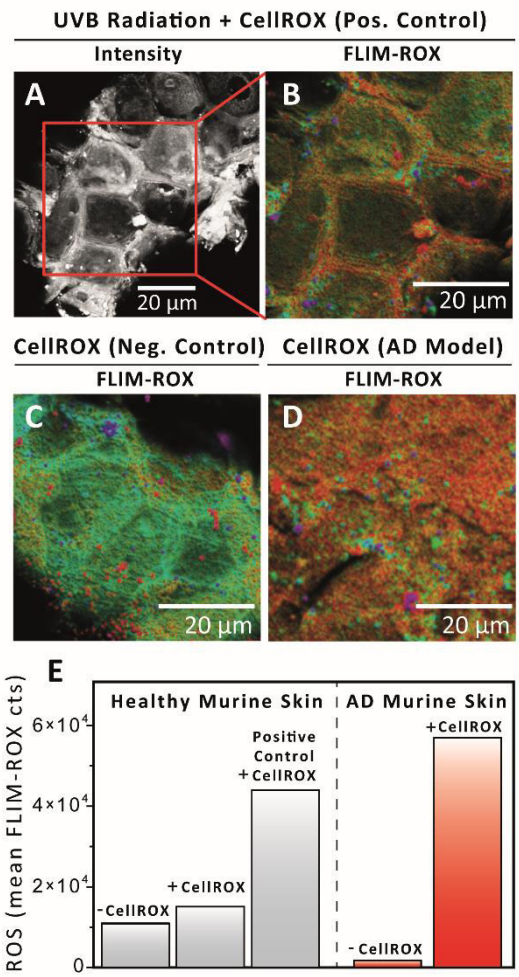

Figure 6. Quantification of ROS levels by multiphoton FLIM-ROX in healthy and atopic dermatitis (AD) model skin. (**A-D**) Stratum corneum (skin depth: 5 µm) of healthy murine skin after 15 min incubation with CellROX Green and UVB irradiation (as positive control) with (**A**) intensity based image and (**B**) FLIM-ROX image, color-coded according to the cluster-based FLIM analysis. Red colored areas indicate the fluorescence lifetime signature of activated CellROX Green, and thus high ROS levels. (**C**) FLIM-ROX image of healthy murine skin with CellROX Green and without irradiation (as negative control). (**D**) FLIM-ROX image of AD model skin with CellROX Green. (**E**) Mean FLIM-ROX intensities in healthy and AD-like murine skin.

AUTHOR INFORMATION

Corresponding Authors

* Ulrike Alexiev: ulrike.alexiev@fu-berlin.de, * Nan Ma: nan.ma@hzg.de

Author Contributions

‡These authors contributed equally.

Funding Sources

German Research Foundation, Collaborative Research Center SFB1112, SFB 1078

Helmholtz Virtual Institute-Multifunctional Biomaterials for Medicine.

ACKNOWLEDGMENT

Financial support by the German Research Foundation (Collaborative Research Center SFB 1112, Project B03 to UA, C03 to ADG and LM, and Z01 to NM) is gratefully acknowledged This work was also partially supported by the Collaborative Research Center SFB 1078, Project A2 to UA. The authors would like to acknowledge the Helmholtz Association through the Helmholtz Virtual Institute-Multifunctional Biomaterials for Medicine.

ABBREVIATIONS

ROS, reactive oxygen species; FLIM, fluorescence lifetime image microscopy; $O_2^{\bullet-}$, superoxide; H_2O_2, hydrogen peroxide ; $OH^{\bullet}$, hydroxyl radical; DCF, dichlorodihydrofluorescein; DHE, dihydroethidium; NADH, 1,4-dihydronicotinamide adenine dinucleotide; TCSPC, time-correlated single photon counting; DNA, deoxyribonucleic acid; AuNP, gold nanoparticles; I_{max}, maximum

intensity in the saturation limit; $c_{1/2}$, concentration needed to reach half saturation; AD, atopic dermatitis; UVB, ultraviolet B; PBS, phosphate-buffered saline; NaOH, sodium hydroxide; EDTA, ethylenediaminetetraacetic acid; FBS, fetal bovine serum; DMEM, Dulbecco's modified Eagle's medium; IRF, instrument response function; FWHM, full-width half-maximum; CLSM, confocal laser scanning microscopy; AOTF, acousto-optical tunable filter; PMT, photo-multiplier tube; DMSO, dimethyl sulfoxide; FOV,field of view; PBMC, primary blood mononuclear cells; CD11b, integrin alpha M; CD14, cluster of differentiation 14; CD206, mannose receptor cluster of differentiation 206; CD1a, cluster of differentiation 1a; CCK-8, cell counting kit 8; mpFLIM, multi photon fluorescence lifetime image microscopy

REFERENCES

1. Napierska, D.; Rabolli, V.; Thomassen, L. C. J.; Dinsdale, D.; Princen, C.; Gonzalez, L.; Poels, K. L. C.; Kirsch-Volders, M.; Lison, D.; Martens, J. A.; Hoet, P. H., Oxidative Stress Induced by Pure and Iron-Doped Amorphous Silica Nanoparticles in Subtoxic Conditions. *Chem. Res. Toxicol.* **2012,** *25*, 828-837.

2. Fu, P. P.; Xia, Q.; Hwang, H.-M.; Ray, P. C.; Yu, H., Mechanisms of Nanotoxicity: Generation of Reactive Oxygen Species. *J. Food Drug Anal.* **2014,** *22*, 64-75.

3. D'Autreaux, B.; Toledano, M. B., ROS as Signalling Molecules: Mechanisms that Generate Specificity in ROS Homeostasis. *Nat. Rev. Mol. Cell Biol.* **2007,** *8*, 813-824.

4. Martindale, J. L.; Holbrook, N. J., Cellular Response to Oxidative Stress: Signaling for Suicide and Survival. *J. Cell. Physiol.* **2002,** *192*, 1-15.

5. Munnamalai, V.; Suter, D. M., Reactive Oxygen Species Regulate F-actin Dynamics in Neuronal Growth Cones and Neurite Outgrowth. *J. Neurochem.* **2009,** *108*, 644-661.

6. Vatansever, F.; de Melo, W. C. M. A.; Avci, P.; Vecchio, D.; Sadasivam, M.; Gupta, A.; Chandran, R.; Karimi, M.; Parizotto, N. A.; Yin, R.; Tegos, G. P.; Hamblin, M. R., Antimicrobial Strategies Centered around Reactive Oxygen Species - Bactericidal Antibiotics, Photodynamic Therapy, and Beyond. *FEMS Microbiol. Rev.* **2013,** *37*, 955-989.

7. Ji, H.; Li, X. K., Oxidative Stress in Atopic Dermatitis. *Oxid. Med. Cell. Longevity* **2016,** *2016*, 2721469.

8. Halliwell, B.; Whiteman, M., Measuring Reactive Species and Oxidative Damage in vivo and in Cell Culture: How should You Do it and What do the Results Mean? *Br. J. Pharmacol.* **2004,** *142*, 231-255.

9. Winterbourn, C. C., The Challenges of Using Fluorescent Probes to Detect and Quantify Specific Reactive Oxygen Species in Living Cells. *Biochim. Biophys. Acta, Gen. Subj.* **2014,** *1840*, 730-738.

10. Fan, L. M.; Li, J. M., Evaluation of Methods of Detecting Cell Reactive Oxygen Species Production for Drug Screening and Cell Cycle Studies. *J. Pharmacol. Toxicol. Methods* **2014,** *70*, 40-47.

11. Woolley, J. F.; Stanicka, J.; Cotter, T. G., Recent Advances in Reactive Oxygen Species Measurement in Biological Systems. *Trends Biochem. Sci.* **2013,** *38*, 556-565.

12. Kalyanaraman, B.; Darley-Usmar, V.; Davies, K. J. A.; Dennery, P. A.; Forman, H. J.; Grisham, M. B.; Mann, G. E.; Moore, K.; Roberts, L. J.; Ischiropoulos, H., Measuring Reactive

Oxygen and Nitrogen Species with Fluorescent Probes: Challenges and Limitations. *Free Radical Biol. Med.* **2012,** *52*, 1-6.

13. Volz, P.; Schilrreff, P.; Brodwolf, R.; Wolff, C.; Stellmacher, J.; Balke, J.; Morilla, M. J.; Zoschke, C.; Schäfer-Korting, M.; Alexiev, U., Pitfalls in Using Fluorescence Tagging of Nanomaterials: Tecto-dendrimers in Skin Tissue as Investigated by Cluster-FLIM. *Ann. N. Y. Acad. Sci.* **2017,** *1405*, 202-214.

14. Alam, S. R.; Wallrabe, H.; Svindrych, Z.; Chaudhary, A. K.; Christopher, K. G.; Chandra, D.; Periasamy, A., Investigation of Mitochondrial Metabolic Response to Doxorubicin in Prostate Cancer Cells: An NADH, FAD and Tryptophan FLIM Assay. *Sci. Rep.* **2017,** *7*, 10451.

15. Bhattacharjee, A.; Datta, R.; Gratton, E.; Hochbaum, A. I., Metabolic fingerprinting of bacteria by fluorescence lifetime imaging microscopy. *Sci. Rep.* **2017,** *7*, 3743.

16. Blacker, T. S.; Mann, Z. F.; Gale, J. E.; Ziegler, M.; Bain, A. J.; Szabadkai, G.; Duchen, M. R., Separating NADH and NADPH Fluorescence in Live Cells and Tissues using FLIM. *Nat. Commun.* **2014,** *5*, 3936.

17. Vittorio, O.; Brandl, M.; Cirillo, G.; Kimpton, K.; Hinde, E.; Gaus, K.; Yee, E.; Kumar, N.; Duong, H.; Fleming, C.; Haber, M.; Norris, M.; Boyer, C.; Kavallaris, M., Dextran-Catechin: An Anticancer Chemically-modified Natural Compound Targeting Copper that Attenuates Neuroblastoma Growth. *Oncotarget* **2016,** *7*, 47479-47493.

18. Datta, R.; Heylman, C.; George, S. C.; Gratton, E., Label-free Imaging of Metabolism and Oxidative Stress in Human Induced Pluripotent Stem Cell-derived Cardiomyocytes. *Biomed. Opt. Express* **2016,** *7*, 1690-1701.

19. Castro, F. A. V.; Mariani, D.; Panek, A. D.; Eleutherio, E. C. A.; Pereira, M. D., Cytotoxicity Mechanism of Two Naphthoquinones (Menadione and Plumbagin) in Saccharomyces cerevisiae. *PLoS One* **2008,** *3*, e3999.

20. Whang, C. H.; Kim, K. S.; Bae, J.; Chen, J.; Jun, H. W.; Jo, S., Novel Biodegradable Polymer with Redox-Triggered Backbone Cleavage Through Sequential 1,6-Elimination and 1,5-Cyclization Reactions. *Macromol. Rapid Commun.* **2017,** *38*.

21. Daum, S.; Reshetnikov, M. S. V.; Sisa, M.; Dumych, T.; Lootsik, M. D.; Bilyy, R.; Bila, E.; Janko, C.; Alexiou, C.; Herrmann, M.; Sellner, L.; Mokhir, A., Lysosome-Targeting Amplifiers of Reactive Oxygen Species as Anticancer Prodrugs. *Angew. Chem., Int. Ed. Engl.* **2017,** *56*, 15545-15549.

22. Kirchberg, K.; Kim, T. Y.; Moller, M.; Skegro, D.; Raju, G. D.; Granzin, J.; Buldt, G.; Schlesinger, R.; Alexiev, U., Conformational Dynamics of Helix 8 in the GPCR Rhodopsin Controls Arrestin Activation in the Desensitization Process. *Proc. Natl. Acad. Sci. U. S. A.* **2011,** *108*, 18690-18695.

23. Boreham, A.; Kim, T. Y.; Spahn, V.; Stein, C.; Mundhenk, L.; Gruber, A. D.; Haag, R.; Welker, P.; Licha, K.; Alexiev, U., Exploiting Fluorescence Lifetime Plasticity in FLIM: Target Molecule Localization in Cells and Tissues. *ACS Med. Chem. Lett.* **2011,** *2*, 724-728.

24. Hoffmann, K.; Behnke, T.; Drescher, D.; Kneipp, J.; Resch-Genger, U., Near-Infrared-Emitting Nanoparticles for Lifetime-Based Multiplexed Analysis and Imaging of Living Cells. *ACS Nano* **2013,** *7*, 6674-6684.

25. Heinrich, R.; Neel, B. G.; Rapoport, T. A., Mathematical Models of Protein Kinase Signal Transduction. *Mol. Cell* **2002,** *9*, 957-970.

26. Antunes, F.; Cadenas, E., Estimation of H_2O_2 Gradients Across Biomembranes. *FEBS Lett.* **2000,** *475*, 121-126.

27. Choi, H.; Yang, Z.; Weisshaar, J. C., Single-cell, Real-time Detection of Oxidative Stress Induced in Escherichia Coli by the Antimicrobial Peptide CM15. *Proc. Natl. Acad. Sci. U. S. A.* **2015,** *112*, E303-E310.

28. de Castro, L. S.; de Assis, P. M.; Siqueira, A. F. P.; Hamilton, T. R. S.; Mendes, C. M.; Losano, J. D. A.; Nichi, M.; Visintin, J. A.; Assumpcao, M. E. O. A., Sperm Oxidative Stress Is Detrimental to Embryo Development: A Dose-Dependent Study Model and a New and More Sensitive Oxidative Status Evaluation. *Oxid. Med. Cell. Longevity* **2016,** *2016*, 8213071.

29. Li, J. J.; Hartono, D.; Ong, C. N.; Bay, B. H.; Yung, L. Y. L., Autophagy and oxidative stress associated with gold nanoparticles. *Biomaterials* **2010,** *31*, 5996-6003.

30. Hanson, K. M.; Clegg, R. M., Observation and Quantification of Ultraviolet-induced Reactive Oxygen Species in ex vivo Human Skin. *Photochem. Photobiol.* **2002,** *76*, 57-63.

31. Alexiev, U.; Rimke, I.; Pohlmann, T., Elucidation of the Nature of the Conformational Changes of the EF-interhelical Loop in Bacteriorhodopsin and of the Helix VIII on the Cytoplasmic Surface of Bovine Rhodopsin: A Time-resolved Fluorescence Depolarization Study. *J. Mol. Biol.* **2003,** *328*, 705-719.

32. Kim, T. Y.; Winkler, K.; Alexiev, U., Picosecond Multidimensional Fluorescence Spectroscopy: A Tool to Measure Real-time Protein Dynamics during Function. *Photochem. Photobiol.* **2007,** *83*, 378-384.

33. Alexiev, U.; Volz, P.; Boreham, A.; Brodwolf, R., Time-resolved Fluorescence Microscopy (FLIM) as an Analytical Tool in Skin Nanomedicine. *Eur. J. Pharm. Biopharm.* **2017,** *116*, 111-124.

34. Radbruch, M.; Pischon, H.; Ostrowski, A.; Volz, P.; Brodwolf, R.; Neumann, F.; Unbehauen, M.; Kleuser, B.; Haag, R.; Ma, N.; Alexiev, U.; Mundhenk, L.; Gruber, A. D., Dendritic Core-Multishell Nanocarriers in Murine Models of Healthy and Atopic Skin. *Nanoscale Res. Lett.* **2017,** *12*.

Table of Contents graphic

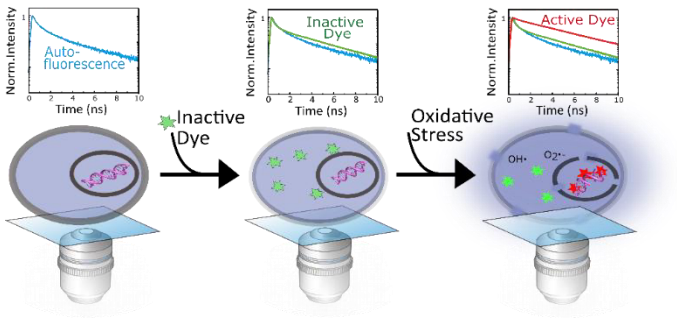

4 Conclusions and Outlook

The goals of this work were the development of new cationic carrier systems that are able to transport sensitive nucleic acid cargo into cells while at the same time decreasing their adverse effects. This was realized with the use of PG as the polymeric backbone of the carrier systems and a cleavable linker that enables the particles biodegradability in the cytosol and also a release of the cargo material.

The first project was a systematic approach to find a best candidate in the frame of hyperbranched polyglycerol nanocarriers by tweaking both the size and the hydroxyl-to-amino ratio on the particle surface. The particles were tested for their performance to transfect plasmid DNA *in vitro*. Among several candidates, PG with a size of 14 kDa and 90 % of amine surface groups and PG 200 kDa with 30 % amine groups were the most promising candidates. These findings are in accord with those of Zeng *et al*., where 14 kDa particles worked best with 50 % amines and 55 kDa particles worked best with 35 % amines for siRNA delivery. The best candidate with similar transfection efficacies as PEI, 200 kDa HPG and 30 % amines, were further studied to elaborate their exact mechanism of toxicity. Compared to 25 kDa branched PEI (bPEI), the cell viability was less affected. Additional tests revealed no evidence for apoptosis but a slight membrane disruption which was more prominent in PEI than in the HPG.

In the second project, micelles based on lipoic acid and PG were combined with a redox sensitive disulfide crosslinker for the delivery of siRNA. All biocompatible building blocks were selected so that there will be no toxicity upon particle degradation and four different structure were generated. Acceptable cell viabilities (> 70 %) were observed for all but one construct up to an N/P ratio of 120. One of the three candidates showed comparable transfection efficacy to the commercial control Lipofectamine® but was still lower. Two other approaches featured the efficacy of different PG polymer structures for transfection: hyperbranched PG with an amine shell and a PG nanogel with small 600 Da PEI units. Both these systems incorporated a pH sensitive cleavable linker. The HPG carriers contained a cleavable linker (50 % cleaved after 12 hours) and a fast-cleavable variety of that (50 % cleaved after 4 hours). The cell viability of the non-degradable carrier and the two degradable ones was comparable and the cleavable one also showed similar transfection efficacy. However, the fast-cleavable carriers showed a decreased performance, indicating that the degradation process needs to be delayed for efficient transfection. The other benzacetal-linker system was a crosslinked nanogel comprising

linear PG and small linear PEI molecules. This system was able to physically encapsulate siRNA during the synthesis process and showed a transfection efficacy similar to that of 25 kDa bPEI. Also, the cell viability was higher, especially at higher concentrations and a subsequent test using red blood cells showed high biocompatibility with biological membranes, whereas PEI showed a visible disruptive effect. The nanogel approach also eliminated the need for complexation of nucleic acids and the carrier system prior to application, making them more feasible in practical use. This feature and the increased biocompatibility makes these system promising candidates for further in vivo tests.

Another project focused on the sensitive detection of reactive oxygen species upon nanoparticle exposure. For this, fluorescence lifetime imaging microscopy (FLIM) was utilized because it increased the sensitivity of the commercial CellROX Green® dye. Calibration curves proved the high functionality of the method in fixed and live cells. Further studies on *ex vivo* skin tissue demonstrated the methods applicability for more complex systems. Also, to consolidate the picture that the ROS generation by model particles made of bioinert gold with an amine shell, other biological studies were performed. These studies revealed induction of cellular senescence and genotoxic effect at subtoxic concentrations as determined by cell viability studies. The results confirm the overall picture of cationic nanoparticle induced adverse effects on cells and legitimate this FLIM method for further routine application for toxicological tests.

For the future, these polycationic nanoparticle delivery system will be further explored for their *in vitro* and *in vivo* application of nucleic acid delivery, or gene delivery, and the delivery of other drugs. The challenge of outperforming viral carrier systems or decreasing the adverse effects completely have not yet been entirely accomplished. Further work will be done on the nanogels due to their flexible size range and the ability to encapsulate a great variety of different cargoes. Also, the interactions of nanoparticles and cells regarding adverse effects needs to be further elucidated. As a sensitive method for the detection of ROS was established in the last project using FLIM, further effort can be taken to eliminate subtoxic oxidative stress and possibly outperform current drug delivery systems.

5 Kurzzusammenfassung

Das Ziel dieser Arbeit bestand aus der Entwicklung kationischer Nanopartikel-Trägersysteme, die in der Lage sind, sensible Gast-Moleküle wie Nukleinsäuren in Zellen zu transportieren und gleichzeitig ihre adversen Effekte zu reduzieren. Realisiert wurde das durch die Verwendung von Polyglycerin als Polymergrundlage des Trägersystems und spaltbarer, Stimuli-responsiver Querverbindungen. Diese ermöglichten die Bioabbaubarkeit der Partikel im Zytosol und den Lysosomen und die Freisetzung der Gastmoleküle.

Das erste Projekt bestand aus einer systematischen Herangehensweise, um das beste Konstrukt eines hochverzweigten, Polyglycerin-basierten Nanoträgers zu finden. Hierzu wurden sowohl die Größe als auch das Verhältnis von Hydroxyl- zu Aminogruppen auf der Partikeloberfläche moduliert. Anschließen wurden die Partikel auf ihr Fähigkeit getestet, *in vitro* Plasmid DNA in Zellen zu transfizieren. Unter mehreren Kandidaten stellten sich PG mit einer Größe von 14 kDa mit 90 % Aminogruppen und 200 kDa mit 30 % Aminogruppen als die besten heraus. Damit konnten die Ergebnisse von Zeng et al bestätigt werden, wonach 14 kDa Partikel mit 50 % Aminogruppen und 55 kDa partikel mit 35 % Aminogruppen am besten für die Transfektion von siRNA geeignet waren.[152] Der beste Kandidat mit einer vergleichbaren Transfektionseffizienz wie PEI, 200 kDa HPG mit 30 % Aminogruppen, wurde des Weiteren auf die Mechanismen der Toxizität geprüft. Im Vergleich zu 25 kDa bPEI (bPEI) war die Zellviabilität allgemein weniger beeinträchtigt. Zusätzliche Tests zeigten keine Anzeichen von Apoptose-Induktion, aber eine leichte Störung der Membranintegrität, wobei der Effekt durch PEI deutlicher ausgeprägt war.

Im zweiten Projekt wurden Liponsäure und PG mit einer redox-sensitiven Verknüpfung kombiniert, um siRNA zu transfizieren. Alle Grundbausteine wurden so gewählt, dass bei einer Spaltung keine toxischen Abbauprodukte freigesetzt werden und vier verschiedene Konstrukte untersucht. Für drei von vier Konstrukte wurde eine akzeptable Zellviabilität festgestellt, bis zu einem N/P-Verhältnis von 120. Einer der drei Kandidaten zeigte eine Transfektioneffizienz, die mit der kommerziell erhältlichen Kontrolle Lipofectamine ® vergleichbar war, wenn auch etwas niedriger. Zwei andere Herangehensweisen befassten sich mit der Effizienz anderer PG Polymerkonstrukte für Transfektionen: hochverzweigtes PG mit einer Amin-Schale und ein PG-Nanogel mit kleinen 600 Da PEI Einheiten. Beide Systeme beinhalten eine pH-sensitiven Querverbindung. Die HPG Träger wurden mit einer spaltbaren Queverbindung und einer schnell-spaltbaren Variante davon ausgestattet, wobei 50 % der Träger nach 12 Stunden bzw. 4 Stunden

gespalten wurden. Die Zellviabilität des Trägers ohne spaltbare Querverbindung und dieser beiden Konstrukte waren sehr ähnlich, aber nur das spaltbare zeigte eine vergleichbare Transfektionseffizienz zu dem nicht-spaltbaren. Die schnell-spaltbare Variante allerdings zeigte eine schlechtere Performance, was darauf hindeutet, dass der Spaltungsvorgang für eine effiziente Transfektion langsamer von statten gehen muss. Das andere pH-sensitive, Benzazetal-verknüpfte System bestand aus Nanogelen bestehend aus PG und kleinen, linearen PEI Einheiten. In diesem System konnte siRNA während der Synthese physikalisch eingekapselt werden. Die Transfektioneffizienz dieses Konstrukts war vergleichbar, wenn auch niedriger, mit der von 25 kDa bPEI. Andererseits war die Zellviabilität höher, vor allem bei hohen Konzentrationen. Ein zusätzlicher Test an roten Blutzellen demonstrierte eine hohe Biokompatibilität gegenüber biologischen Membranen, während PEI einen deutlichen schädlichen Effekt zeigte. Der Nanogel-Ansatz als Träger-System eliminiert außerdem die Notwendigkeit für eine Komplexierung von Nukleinsäuren vor der Anwendung, da diese bereits verkapselt sind. Das macht sie in der Anwendung vergleichsweise praktikabel. Insgesamt machen die Vorteile der erhöhten Biokompatibilität und der Einfachheit der Anwendung dieses System zu einem vielversprechenden Kandidaten für spätere *in vivo* Versuche.

Ein anderes Projekt war auf die sensitive Detektion von reaktiven Sauerstoffspeziesfokussiert, welche bei Kontakt mit Nanopartikeln freigesetzt werden können. Dafür wurde der Farbstoff CellROX Green ® in Kombination mit Fluorescence Lifetime Imaging Microscopy (FLIM) verwendet, um dessen Sensitivität zu erhöhen. Durch Kalibrationskurven konnte die Funktionalität der Methode sowohl in fixierten als auch in lebenden Zellen gezeigt werden. Des Weiteren konnte die Anwendbarkeit der Methode für komplexere biologische Systeme anhand von *ex vivo* Versuchen demonstriert werden. Um das Gesamtbild um den gemessen oxidativen Stress zu vervollständigen, wurden Modell-Partikel aus Gold mit einer Amin-Schale verwendet und weitere biologische Untersuchungen durchgeführt. Dazu wurden Zellviabilitätsstudien durchgeführt und subtoxische Konzentrationen verwendet. Diese demonstrierten neben den der Generierung von ROS auch die Induktion von zellulärer Seneszenz und einen genotoxischen Effekt. Die Ergebnisse bestätigten das allgemeine Gesamtbild der adversen Effekte von kationischen Nanopartikeln auf Zellen und legitimierten damit diese neue FLIM-Methode und deren möglichen Einsatz in Routine-Kontrollen im Zusammenhang mit medizinischen Anwendungen.

Für die Zukunft werden diese vielversprechenden kationischen Nanopartikel-Trägersysteme weiter erforscht, sowohl für die Anwendung mit Nukleinsäuren als auch anderen Arzneistoffen und das sowohl *in vitro* als auch *in vivo*. Die Herausforderung, virale Vektorsysteme zu übertreffen oder die adversen Effekte komplett zu eliminieren, ist

noch nicht gemeistert. Weitere Arbeit sollte in die Nanogel-Systeme gesteckt werden, da diese durch ihre flexible Größe und der Möglichkeit zur Einkapselung verschiedenster Arzneimittel ein besonders großen Potential haben. Zusätzlich sollten die Interaktionen zwischen kationischen Nanopartikeln und Zellen sowie die adversen Effekte weiter aufgeklärt werden. Da mit dieser Arbeit eine sensitive Methode für die Messung von ROS mittels FLIM-Technologie etabliert wurde, sollte diese genutzt werden, um die adversen Effekte bei toxischen und subtoxischen Konzentrationen weiter zu eliminieren. Auf lange Sicht könnte das eine aussagekräftige Methode sein, aktuelle Trägersysteme weiter zu untersuchen und zu verbessern.

6 References

1. Ogura, T.; Okada, T., Nanoscale observation of the natural structure of milk-fat globules and casein micelles in the liquid condition using a scanning electron assisted dielectric microscopy. *Biochem Biophys Res Commun* **2017,** *491* (4), 1021-1025.

2. Nel, A.; Xia, T.; Madler, L.; Li, N., Toxic potential of materials at the nanolevel. *Science* **2006,** *311* (5761), 622-627.

3. Park, K., Controlled drug delivery systems: past forward and future back. *J Control Release* **2014,** *190*, 3-8.

4. Barenholz, Y., Doxil(R)--the first FDA-approved nano-drug: lessons learned. *J Control Release* **2012,** *160* (2), 117-34.

5. Leeson, P., Drug discovery: Chemical beauty contest. *Nature* **2012,** *481* (7382), 455-6.

6. Rocha, M.; Chaves, N.; Báo, S., Nanobiotechnology for Breast Cancer Treatment. In *Breast Cancer - From Biology to Medicine*, Pham, P. V., Ed. InTech: Rijeka, 2017; p Ch. 21.

7. Ladj, R.; Bitar, A.; Eissa, M. M.; Fessi, H.; Mugnier, Y.; Le Dantec, R.; Elaissari, A., Polymer encapsulation of inorganic nanoparticles for biomedical applications. *Int J Pharm* **2013,** *458* (1), 230-41.

8. Jeon, I. Y.; Baek, J. B., Nanocomposites Derived from Polymers and Inorganic Nanoparticles. *Materials* **2010,** *3* (6), 3654-3674.

9. Muralidharan, P.; Mallory, E.; Malapit, M.; Hayes, D., Jr.; Mansour, H. M., Inhalable PEGylated Phospholipid Nanocarriers and PEGylated Therapeutics for Respiratory Delivery as Aerosolized Colloidal Dispersions and Dry Powder Inhalers. *Pharmaceutics* **2014,** *6* (2), 333-53.

10. Franze, S.; Marengo, A.; Stella, B.; Minghetti, P.; Arpicco, S.; Cilurzo, F., Hyaluronan-Decorated Liposomes as Drug Delivery Systems for Cutaneous Administration. *Int J Pharm* **2017**.

11. Tan, Y.; Zhu, Y.; Zhao, Y.; Wen, L.; Meng, T.; Liu, X.; Yang, X.; Dai, S.; Yuan, H.; Hu, F., Mitochondrial alkaline pH-responsive drug release mediated by Celastrol loaded glycolipid-like micelles for cancer therapy. *Biomaterials* **2017,** *154*, 169-181.

12. Wang, C.; Ye, X.; Wang, Z.; Wu, T.; Wang, Y.; Li, C., Molecularly Imprinted Photoelectrochemical Sensor for Human Epididymis Protein 4 Based on Polymerized Ionic Liquid Hydrogel and Gold Nanoparticle/ZnCdHgSe Quantum Dots Composite Film. *Anal Chem* **2017**.

13. Park, J.; Pramanick, S.; Kim, J.; Lee, J.; Kim, W. J., Nitric oxide-activatable gold nanoparticles for specific targeting and photo-thermal ablation of macrophages. *Chem Commun (Camb)* **2017,** *53* (81), 11229-11232.

14. Mellaerts, R.; Mols, R.; Jammaer, J. A.; Aerts, C. A.; Annaert, P.; Van Humbeeck, J.; Van den Mooter, G.; Augustijns, P.; Martens, J. A., Increasing the oral bioavailability of

the poorly water soluble drug itraconazole with ordered mesoporous silica. *Eur J Pharm Biopharm* **2008,** *69* (1), 223-30.

15. Ren, X.; Lin, J.; Wang, X.; Liu, X.; Meng, E.; Zhang, R.; Sang, Y.; Zhang, Z., Photoactivatable RNAi for cancer gene therapy triggered by near-infrared-irradiated single-walled carbon nanotubes. *Int J Nanomedicine* **2017,** *12*, 7885-7896.

16. Rabias, I.; Tsitrouli, D.; Karakosta, E.; Kehagias, T.; Diamantopoulos, G.; Fardis, M.; Stamopoulos, D.; Maris, T. G.; Falaras, P.; Zouridakis, N.; Diamantis, N.; Panayotou, G.; Verganelakis, D. A.; Drossopoulou, G. I.; Tsilibari, E. C.; Papavassiliou, G., Rapid magnetic heating treatment by highly charged maghemite nanoparticles on Wistar rats exocranial glioma tumors at microliter volume. *Biomicrofluidics* **2010,** *4* (2).

17. Katas, H.; Raja, M. A.; Lam, K. L., Development of Chitosan Nanoparticles as a Stable Drug Delivery System for Protein/siRNA. *Int J Biomater* **2013,** *2013*, 146320.

18. Ahmad, Z.; Sharma, S.; Khuller, G. K., Inhalable alginate nanoparticles as antitubercular drug carriers against experimental tuberculosis. *Int J Antimicrob Agents* **2005,** *26* (4), 298-303.

19. Loos, C.; Syrovets, T.; Musyanovych, A.; Mailander, V.; Landfester, K.; Nienhaus, G. U.; Simmet, T., Functionalized polystyrene nanoparticles as a platform for studying bio-nano interactions. *Beilstein J Nanotechnol* **2014,** *5*, 2403-12.

20. Arami, S.; Mahdavi, M.; Rashidi, M. R.; Fathi, M.; Hejazi, M. S.; Samadi, N., Novel polyacrylate-based cationic nanoparticles for survivin siRNA delivery combined with mitoxantrone for treatment of breast cancer. *Biologicals* **2016,** *44* (6), 487-496.

21. Nouri, F.; Sadeghpour, H.; Heidari, R.; Dehshahri, A., Preparation, characterization, and transfection efficiency of low molecular weight polyethylenimine-based nanoparticles for delivery of the plasmid encoding CD200 gene. *Int J Nanomedicine* **2017,** *12*, 5557-5569.

22. Rao, K.; Zhong, Q.; Bielski, E. R.; da Rocha, S. R. P., Nanoparticles of pH-Responsive, PEG-Doxorubicin Conjugates: Interaction with an in Vitro Model of Lung Adenocarcinoma and Their Direct Formulation in Propellant-Based Portable Inhalers. *Mol Pharm* **2017,** *14* (11), 3866-3878.

23. Hellmund, M.; Zhou, H.; Samsonova, O.; Welker, P.; Kissel, T.; Haag, R., Functionalized polyglycerol amine nanogels as nanocarriers for DNA. *Macromol Biosci* **2014,** *14* (9), 1215-21.

24. Fleige, E.; Achazi, K.; Schaletzki, K.; Triemer, T.; Haag, R., pH-responsive dendritic core-multishell nanocarriers. *J Control Release* **2014,** *185*, 99-108.

25. Wilhelm, C.; Billotey, C.; Roger, J.; Pons, J. N.; Bacri, J. C.; Gazeau, F., Intracellular uptake of anionic superparamagnetic nanoparticles as a function of their surface coating. *Biomaterials* **2003,** *24* (6), 1001-11.

26. Verma, A.; Stellacci, F., Effect of surface properties on nanoparticle-cell interactions. *Small* **2010,** *6* (1), 12-21.

27. Flannagan, R. S.; Jaumouillé, V.; Grinstein, S., The Cell Biology of Phagocytosis. *Annual Review of Pathology: Mechanisms of Disease* **2012,** *7* (1), 61-98.

28. Kettiger, H.; Schipanski, A.; Wick, P.; Huwyler, J., Engineered nanomaterial uptake and tissue distribution: from cell to organism. *Int J Nanomedicine* **2013,** *8*, 3255-69.

29. Lesniak, A.; Campbell, A.; Monopoli, M. P.; Lynch, I.; Salvati, A.; Dawson, K. A., Serum heat inactivation affects protein corona composition and nanoparticle uptake. *Biomaterials* **2010,** *31* (36), 9511-8.

30. Rejman, J.; Oberle, V.; Zuhorn, I. S.; Hoekstra, D., Size-dependent internalization of particles via the pathways of clathrin- and caveolae-mediated endocytosis. *Biochem J* **2004,** *377* (Pt 1), 159-69.

31. Parton, R. G.; Simons, K., The multiple faces of caveolae. *Nat Rev Mol Cell Biol* **2007,** *8* (3), 185-94.

32. Wang, Z.; Tiruppathi, C.; Minshall, R. D.; Malik, A. B., Size and dynamics of caveolae studied using nanoparticles in living endothelial cells. *ACS Nano* **2009,** *3* (12), 4110-6.

33. Marks, B.; Stowell, M. H. B.; Vallis, Y.; Mills, I. G.; Gibson, A.; Hopkins, C. R.; McMahon, H. T., GTPase activity of dynamin and resulting conformation change are essential for endocytosis. *Nature* **2001,** *410*, 231.

34. Sahay, G.; Alakhova, D. Y.; Kabanov, A. V., Endocytosis of nanomedicines. *J Control Release* **2010,** *145* (3), 182-95.

35. Mercer, J.; Schelhaas, M.; Helenius, A., Virus Entry by Endocytosis. *Annual Review of Biochemistry* **2010,** *79* (1), 803-833.

36. Kuhn, D. A.; Vanhecke, D.; Michen, B.; Blank, F.; Gehr, P.; Petri-Fink, A.; Rothen-Rutishauser, B., Different endocytotic uptake mechanisms for nanoparticles in epithelial cells and macrophages. *Beilstein J Nanotechnol* **2014,** *5*, 1625-36.

37. Diaz-Moscoso, A.; Vercauteren, D.; Rejman, J.; Benito, J. M.; Ortiz Mellet, C.; De Smedt, S. C.; Fernandez, J. M., Insights in cellular uptake mechanisms of pDNA-polycationic amphiphilic cyclodextrin nanoparticles (CDplexes). *J Control Release* **2010,** *143* (3), 318-25.

38. Le Bihan, O.; Bonnafous, P.; Marak, L.; Bickel, T.; Trepout, S.; Mornet, S.; De Haas, F.; Talbot, H.; Taveau, J. C.; Lambert, O., Cryo-electron tomography of nanoparticle transmigration into liposome. *J Struct Biol* **2009,** *168* (3), 419-25.

39. Tatur, S.; Maccarini, M.; Barker, R.; Nelson, A.; Fragneto, G., Effect of functionalized gold nanoparticles on floating lipid bilayers. *Langmuir* **2013,** *29* (22), 6606-14.

40. Harush-Frenkel, O.; Debotton, N.; Benita, S.; Altschuler, Y., Targeting of nanoparticles to the clathrin-mediated endocytic pathway. *Biochem Biophys Res Commun* **2007,** *353* (1), 26-32.

41. Chung, T. H.; Wu, S. H.; Yao, M.; Lu, C. W.; Lin, Y. S.; Hung, Y.; Mou, C. Y.; Chen, Y. C.; Huang, D. M., The effect of surface charge on the uptake and biological function of mesoporous silica nanoparticles in 3T3-L1 cells and human mesenchymal stem cells. *Biomaterials* **2007,** *28* (19), 2959-66.

42. Rejman, J.; Bragonzi, A.; Conese, M., Role of clathrin- and caveolae-mediated endocytosis in gene transfer mediated by lipo- and polyplexes. *Mol Ther* **2005,** *12* (3), 468-74.

43. Chen, K. L.; Bothun, G. D., Nanoparticles meet cell membranes: probing nonspecific interactions using model membranes. *Environ Sci Technol* **2014,** *48* (2), 873-80.

44. Kiss, A. L.; Botos, E., Endocytosis via caveolae: alternative pathway with distinct cellular compartments to avoid lysosomal degradation? *J Cell Mol Med* **2009,** *13* (7), 1228-37.

45. Mindell, J. A., Lysosomal acidification mechanisms. *Annu Rev Physiol* **2012,** *74*, 69-86.

46. Liang, W.; Lam, J. K. W., Endosomal Escape Pathways for Non-Viral Nucleic Acid Delivery Systems. In *Molecular Regulation of Endocytosis*, Ceresa, B., Ed. InTech: Rijeka, 2012; p Ch. 17.

47. Sonawane, N. D.; Szoka, F. C., Jr.; Verkman, A. S., Chloride accumulation and swelling in endosomes enhances DNA transfer by polyamine-DNA polyplexes. *J Biol Chem* **2003,** *278* (45), 44826-31.

48. Benjaminsen, R. V.; Mattebjerg, M. A.; Henriksen, J. R.; Moghimi, S. M.; Andresen, T. L., The possible "proton sponge " effect of polyethylenimine (PEI) does not include change in lysosomal pH. *Mol Ther* **2013,** *21* (1), 149-57.

49. Bieber, T.; Meissner, W.; Kostin, S.; Niemann, A.; Elsasser, H. P., Intracellular route and transcriptional competence of polyethylenimine-DNA complexes. *J Control Release* **2002,** *82* (2-3), 441-54.

50. Varkouhi, A. K.; Scholte, M.; Storm, G.; Haisma, H. J., Endosomal escape pathways for delivery of biologicals. *J Control Release* **2011,** *151* (3), 220-8.

51. Gerson, F.; Haselbac.E; Plattner, G., Radical Anion of 1,8-Bis(Dimethylamino)Naphthalene (Proton Sponge). *Chem Phys Lett* **1971,** *12* (2), 316-&.

52. Yazeji, T.; Moulari, B.; Beduneau, A.; Stein, V.; Dietrich, D.; Pellequer, Y.; Lamprecht, A., Nanoparticle-based delivery enhances anti-inflammatory effect of low molecular weight heparin in experimental ulcerative colitis. *Drug Deliv* **2017,** *24* (1), 811-817.

53. Wolff, J. A.; Lederberg, J., An early history of gene transfer and therapy. *Hum Gene Ther* **1994,** *5* (4), 469-80.

54. Cavazzana-Calvo, M.; Hacein-Bey, S.; de Saint Basile, G.; Gross, F.; Yvon, E.; Nusbaum, P.; Selz, F.; Hue, C.; Certain, S.; Casanova, J. L.; Bousso, P.; Deist, F. L.; Fischer, A., Gene therapy of human severe combined immunodeficiency (SCID)-X1 disease. *Science* **2000,** *288* (5466), 669-72.

55. Zou, W.; Liu, C.; Chen, Z.; Zhang, N., Preparation and Characterization of Cationic PLA-PEG Nanoparticles for Delivery of Plasmid DNA. *Nanoscale Res Lett* **2009,** *4* (9), 982-992.

56. Thomas, M.; Lu, J. J.; Zhang, C.; Chen, J.; Klibanov, A. M., Identification of novel superior polycationic vectors for gene delivery by high-throughput synthesis and screening of a combinatorial library. *Pharm Res* **2007,** *24* (8), 1564-71.

57. Patnaik, S.; Gupta, K. C., Novel polyethylenimine-derived nanoparticles for in vivo gene delivery. *Expert Opin Drug Deliv* **2013,** *10* (2), 215-28.

58. Barnaby, S. N.; Lee, A.; Mirkin, C. A., Probing the inherent stability of siRNA immobilized on nanoparticle constructs. *Proc Natl Acad Sci U S A* **2014,** *111* (27), 9739-44.

59. Carthew, R. W.; Sontheimer, E. J., Origins and Mechanisms of miRNAs and siRNAs. *Cell* **2009,** *136* (4), 642-55.

60. Leachman, S. A.; Hickerson, R. P.; Hull, P. R.; Smith, F. J.; Milstone, L. M.; Lane, E. B.; Bale, S. J.; Roop, D. R.; McLean, W. H.; Kaspar, R. L., Therapeutic siRNAs for dominant genetic skin disorders including pachyonychia congenita. *J Dermatol Sci* **2008,** *51* (3), 151-7.

61. Liang, Y.; Liu, Z.; Shuai, X.; Wang, W.; Liu, J.; Bi, W.; Wang, C.; Jing, X.; Liu, Y.; Tao, E., Delivery of cationic polymer-siRNA nanoparticles for gene therapies in neural regeneration. *Biochem Biophys Res Commun* **2012,** *421* (4), 690-5.

62. Li, J.; Xue, S.; Mao, Z.-W., Nanoparticle delivery systems for siRNA-based therapeutics. *J Mater Chem B* **2016,** *4* (41), 6620-6639.

63. Ling, H.; Fabbri, M.; Calin, G. A., MicroRNAs and other non-coding RNAs as targets for anticancer drug development. *Nat Rev Drug Discov* **2013,** *12* (11), 847-65.

64. Babar, I. A.; Cheng, C. J.; Booth, C. J.; Liang, X.; Weidhaas, J. B.; Saltzman, W. M.; Slack, F. J., Nanoparticle-based therapy in an in vivo microRNA-155 (miR-155)-dependent mouse model of lymphoma. *Proc Natl Acad Sci U S A* **2012,** *109* (26), E1695-704.

65. Chiou, G. Y.; Cherng, J. Y.; Hsu, H. S.; Wang, M. L.; Tsai, C. M.; Lu, K. H.; Chien, Y.; Hung, S. C.; Chen, Y. W.; Wong, C. I.; Tseng, L. M.; Huang, P. I.; Yu, C. C.; Hsu, W. H.; Chiou, S. H., Cationic polyurethanes-short branch PEI-mediated delivery of Mir145 inhibited epithelial-mesenchymal transdifferentiation and cancer stem-like properties and in lung adenocarcinoma. *J Control Release* **2012,** *159* (2), 240-50.

66. Reis, C. P.; Neufeld, R. J.; Ribeiro, A. J.; Veiga, F., Nanoencapsulation I. Methods for preparation of drug-loaded polymeric nanoparticles. *Nanomedicine* **2006,** *2* (1), 8-21.

67. Florea, B. I.; Meaney, C.; Junginger, H. E.; Borchard, G., Transfection efficiency and toxicity of polyethylenimine in differentiated Calu-3 and nondifferentiated COS-1 cell cultures. *AAPS PharmSci* **2002,** *4* (3), E12.

68. Breunig, M.; Lungwitz, U.; Liebl, R.; Goepferich, A., Breaking up the correlation between efficacy and toxicity for nonviral gene delivery. *Proc Natl Acad Sci U S A* **2007,** *104* (36), 14454-9.

69. Choi, Y. J.; Kang, S. J.; Kim, Y. J.; Lim, Y. B.; Chung, H. W., Comparative studies on the genotoxicity and cytotoxicity of polymeric gene carriers polyethylenimine (PEI) and polyamidoamine (PAMAM) dendrimer in Jurkat T-cells. *Drug Chem Toxicol* **2010,** *33* (4), 357-66.

70. Sherman, R. B.; Woodcock, J.; Norden, J.; Grandinetti, C.; Temple, R. J., New FDA regulation to improve safety reporting in clinical trials. *N Engl J Med* **2011,** *365* (1), 3-5.

71. Dent, N. J., The inspection of drug metabolism and pharmacokinetic studies. *Qual Assur* **1992,** *1* (3), 230-6.

72. Thomas D.Y. Chung, D. B. T., and Layton H. Smith., In Vitro and In Vivo Assessment of ADME and PK Properties During Lead Selection and Lead Optimization – Guidelines, Benchmarks and Rules of Thumb. *Sittampalam GS, Coussens NP, Brimacombe K, et al., editors. Assay Guidance Manual [Internet]. Bethesda (MD): Eli Lilly & Company and the National Center for Advancing Translational Sciences; 2004-.* **2015**.

73. Teeguarden, J. G.; Hinderliter, P. M.; Orr, G.; Thrall, B. D.; Pounds, J. G., Particokinetics in vitro: dosimetry considerations for in vitro nanoparticle toxicity assessments. *Toxicol Sci* **2007,** *95* (2), 300-12.

74. Kim, I. Y.; Joachim, E.; Choi, H.; Kim, K., Toxicity of silica nanoparticles depends on size, dose, and cell type. *Nanomedicine* **2015,** *11* (6), 1407-16.

75. Sharma, A.; Madhunapantula, S. V.; Robertson, G. P., Toxicological considerations when creating nanoparticle-based drugs and drug delivery systems. *Expert Opin Drug Metab Toxicol* **2012,** *8* (1), 47-69.

76. Ehlerding, E. B.; Chen, F.; Cai, W., Biodegradable and Renal Clearable Inorganic Nanoparticles. *Adv Sci (Weinh)* **2016,** *3* (2).

77. Sakhtianchi, R.; Minchin, R. F.; Lee, K. B.; Alkilany, A. M.; Serpooshan, V.; Mahmoudi, M., Exocytosis of nanoparticles from cells: role in cellular retention and toxicity. *Adv Colloid Interface Sci* **2013,** *201-202*, 18-29.

78. Tlotleng, N.; Vetten, M. A.; Keter, F. K.; Skepu, A.; Tshikhudo, R.; Gulumian, M., Cytotoxicity, intracellular localization and exocytosis of citrate capped and PEG functionalized gold nanoparticles in human hepatocyte and kidney cells. *Cell Biology and Toxicology* **2016,** *32* (4), 305-321.

79. Donaldson, K.; Brown, D.; Clouter, A.; Duffin, R.; MacNee, W.; Renwick, L.; Tran, L.; Stone, V., The pulmonary toxicology of ultrafine particles. *J Aerosol Med* **2002,** *15* (2), 213-20.

80. Oberdorster, G.; Oberdorster, E.; Oberdorster, J., Nanotoxicology: an emerging discipline evolving from studies of ultrafine particles. *Environ Health Perspect* **2005,** *113* (7), 823-39.

81. Choi, H. S.; Ashitate, Y.; Lee, J. H.; Kim, S. H.; Matsui, A.; Insin, N.; Bawendi, M. G.; Semmler-Behnke, M.; Frangioni, J. V.; Tsuda, A., Rapid translocation of nanoparticles from the lung airspaces to the body. *Nat Biotechnol* **2010,** *28* (12), 1300-3.

82. Shakeel, M.; Jabeen, F.; Shabbir, S.; Asghar, M. S.; Khan, M. S.; Chaudhry, A. S., Toxicity of Nano-Titanium Dioxide (TiO2-NP) Through Various Routes of Exposure: a Review. *Biological Trace Element Research* **2016,** *172* (1), 1-36.

83. Monteiro-Riviere, N. A.; Filon, F. L., Chapter 11 - Skin A2 - Fadeel, Bengt. In *Adverse Effects of Engineered Nanomaterials*, Pietroiusti, A.; Shvedova, A. A., Eds. Academic Press: Boston, 2012; pp 185-207.

84. Jakoby, W. B.; Ziegler, D. M., The enzymes of detoxication. *J Biol Chem* **1990,** *265* (34), 20715-8.

85. Zhang, Y.; Hu, Z.; Ye, M.; Pan, Y.; Chen, J.; Luo, Y.; Zhang, Y.; He, L.; Wang, J., Effect of poly(ethylene glycol)-block-polylactide nanoparticles on hepatic cells of mouse: low cytotoxicity, but efflux of the nanoparticles by ATP-binding cassette transporters. *Eur J Pharm Biopharm* **2007,** *66* (2), 268-80.

86. Yildirimer, L.; Thanh, N. T.; Loizidou, M.; Seifalian, A. M., Toxicology and clinical potential of nanoparticles. *Nano Today* **2011,** *6* (6), 585-607.

87. Sadauskas, E.; Wallin, H.; Stoltenberg, M.; Vogel, U.; Doering, P.; Larsen, A.; Danscher, G., Kupffer cells are central in the removal of nanoparticles from the organism. *Part Fibre Toxicol* **2007,** *4*, 10.

88. Zhu, S.; Zhang, J.; Zhang, L.; Ma, W.; Man, N.; Liu, Y.; Zhou, W.; Lin, J.; Wei, P.; Jin, P.; Zhang, Y.; Hu, Y.; Gu, E.; Lu, X.; Yang, Z.; Liu, X.; Bai, L.; Wen, L., Inhibition of Kupffer Cell Autophagy Abrogates Nanoparticle-Induced Liver Injury. *Adv Healthc Mater* **2017,** *6* (9).

89. Gustafson, H. H.; Holt-Casper, D.; Grainger, D. W.; Ghandehari, H., Nanoparticle Uptake: The Phagocyte Problem. *Nano Today* **2015,** *10* (4), 487-510.

90. Knudsen, K. B.; Northeved, H.; Kumar, P. E.; Permin, A.; Gjetting, T.; Andresen, T. L.; Larsen, S.; Wegener, K. M.; Lykkesfeldt, J.; Jantzen, K.; Loft, S.; Moller, P.; Roursgaard, M., In vivo toxicity of cationic micelles and liposomes. *Nanomedicine* **2015,** *11* (2), 467-77.

91. Pegg, D. E., Viability assays for preserved cells, tissues, and organs. *Cryobiology* **1989,** *26* (3), 212-31.

92. McNeil, P. L.; Steinhardt, R. A., Loss, restoration, and maintenance of plasma membrane integrity. *J Cell Biol* **1997,** *137* (1), 1-4.

93. McNeil, P. L.; Steinhardt, R. A., Plasma membrane disruption: repair, prevention, adaptation. *Annu Rev Cell Dev Biol* **2003,** *19*, 697-731.

94. Chen, J.; Hessler, J. A.; Putchakayala, K.; Panama, B. K.; Khan, D. P.; Hong, S.; Mullen, D. G.; Dimaggio, S. C.; Som, A.; Tew, G. N.; Lopatin, A. N.; Baker, J. R.; Holl, M. M.; Orr, B. G., Cationic nanoparticles induce nanoscale disruption in living cell plasma membranes. *J Phys Chem B* **2009,** *113* (32), 11179-85.

95. Wang, B.; Zhang, L.; Bae, S. C.; Granick, S., Nanoparticle-induced surface reconstruction of phospholipid membranes. *Proc Natl Acad Sci U S A* **2008,** *105* (47), 18171-5.

96. Stachowiak, J. C.; Hayden, C. C.; Sasaki, D. Y., Steric confinement of proteins on lipid membranes can drive curvature and tubulation. *Proc Natl Acad Sci U S A* **2010,** *107* (17), 7781-6.

97. Li, S.; Malmstadt, N., Deformation and poration of lipid bilayer membranes by cationic nanoparticles. *Soft Matter* **2013,** *9* (20), 4969-4976.

98. Ting, C. L.; Wang, Z. G., Interactions of a charged nanoparticle with a lipid membrane: implications for gene delivery. *Biophys J* **2011,** *100* (5), 1288-97.

99. Florea, B. I.; Meaney, C.; Junginger, H. E.; Borchard, G., Transfection efficiency and toxicity of polyethylenimine in differentiated Calu-3 and nondifferentiated COS-1 cell cultures. *AAPS PharmSci* **2002,** *4* (3), 1-11.

100. Leroueil, P. R.; Hong, S.; Mecke, A.; Baker, J. R., Jr.; Orr, B. G.; Banaszak Holl, M. M., Nanoparticle interaction with biological membranes: does nanotechnology present a Janus face? *Acc Chem Res* **2007,** *40* (5), 335-42.

101. Moghadam, B. Y.; Hou, W. C.; Corredor, C.; Westerhoff, P.; Posner, J. D., Role of nanoparticle surface functionality in the disruption of model cell membranes. *Langmuir* **2012,** *28* (47), 16318-26.

102. Afonso, V.; Champy, R.; Mitrovic, D.; Collin, P.; Lomri, A., Reactive oxygen species and superoxide dismutases: role in joint diseases. *Joint Bone Spine* **2007,** *74* (4), 324-9.

103. Chelikani, P.; Fita, I.; Loewen, P. C., Diversity of structures and properties among catalases. *Cellular and Molecular Life Sciences CMLS* **2004,** *61* (2), 192-208.

104. Hynninen, P. H.; Kaartinen, V.; Kolehmainen, E., Horseradish peroxidase-catalyzed oxidation of chlorophyll a with hydrogen peroxide: characterization of the products and mechanism of the reaction. *Biochim Biophys Acta* **2010,** *1797* (5), 531-42.

105. Deponte, M., Glutathione catalysis and the reaction mechanisms of glutathione-dependent enzymes. *Biochim Biophys Acta* **2013,** *1830* (5), 3217-66.

106. Makino, N.; Mochizuki, Y.; Bannai, S.; Sugita, Y., Kinetic studies on the removal of extracellular hydrogen peroxide by cultured fibroblasts. *J Biol Chem* **1994,** *269* (2), 1020-5.

107. Pacher, P.; Beckman, J. S.; Liaudet, L., Nitric oxide and peroxynitrite in health and disease. *Physiol Rev* **2007,** *87* (1), 315-424.

108. Hayyan, M.; Hashim, M. A.; AlNashef, I. M., Superoxide Ion: Generation and Chemical Implications. *Chem Rev* **2016,** *116* (5), 3029-85.

109. Koppenol, W. H., The Haber-Weiss cycle--70 years later. *Redox Rep* **2001,** *6* (4), 229-34.

110. Valko, M.; Rhodes, C. J.; Moncol, J.; Izakovic, M.; Mazur, M., Free radicals, metals and antioxidants in oxidative stress-induced cancer. *Chem Biol Interact* **2006,** *160* (1), 1-40.

111. Olawale R. Ajuwon, J. L. M. a. L. M. D., Rooibos (Aspalathus linearis) and its Major Flavonoids — Potential Against Oxidative Stress-Induced Conditions, Basic Principles and Clinical Significance of Oxidative Stress, Dr. Sivakumar Joghi Thatha Gowder (Ed.). *InTech* **2015**.

112. Sharma, P.; Jha, A. B.; Dubey, R. S.; Pessarakli, M., Reactive Oxygen Species, Oxidative Damage, and Antioxidative Defense Mechanism in Plants under Stressful Conditions. *Journal of Botany* **2012,** *2012*, 26.

113. Barrera, G., Oxidative stress and lipid peroxidation products in cancer progression and therapy. *ISRN Oncol* **2012,** *2012*, 137289.

114. Barrera, G.; Pizzimenti, S.; Dianzani, M. U., Lipid peroxidation: control of cell proliferation, cell differentiation and cell death. *Mol Aspects Med* **2008,** *29* (1-2), 1-8.

115. Van der Paal, J.; Neyts, E. C.; Verlackt, C. C. W.; Bogaerts, A., Effect of lipid peroxidation on membrane permeability of cancer and normal cells subjected to oxidative stress. *Chem Sci* **2016,** *7* (1), 489-498.

116. Chaudhary, A. K.; Reddy, G. R.; Blair, I. A.; Marnett, L. J., Characterization of an N6-oxopropenyl-2'-deoxyadenosine adduct in malondialdehyde-modified DNA using liquid chromatography/electrospray ionization tandem mass spectrometry. *Carcinogenesis* **1996,** *17* (5), 1167-70.

117. Nam, T. G., Lipid peroxidation and its toxicological implications. *Toxicol Res* **2011,** *27* (1), 1-6.

118. Berlett, B. S.; Stadtman, E. R., Protein oxidation in aging, disease, and oxidative stress. *J Biol Chem* **1997,** *272* (33), 20313-6.

119. Cecarini, V.; Gee, J.; Fioretti, E.; Amici, M.; Angeletti, M.; Eleuteri, A. M.; Keller, J. N., Protein oxidation and cellular homeostasis: Emphasis on metabolism. *Biochim Biophys Acta* **2007,** *1773* (2), 93-104.

120. Ahmad, S.; Khan, H.; Shahab, U.; Rehman, S.; Rafi, Z.; Khan, M. Y.; Ansari, A.; Siddiqui, Z.; Ashraf, J. M.; Abdullah, S. M.; Habib, S.; Uddin, M., Protein oxidation: an overview of metabolism of sulphur containing amino acid, cysteine. *Front Biosci (Schol Ed)* **2017,** *9*, 71-87.

121. Cadet, J.; Wagner, J. R., DNA base damage by reactive oxygen species, oxidizing agents, and UV radiation. *Cold Spring Harb Perspect Biol* **2013,** *5* (2).

122. Jena, N. R., DNA damage by reactive species: Mechanisms, mutation and repair. *J Biosci* **2012,** *37* (3), 503-17.

123. Hong, I. S.; Greenberg, M. M., DNA interstrand cross-link formation initiated by reaction between singlet oxygen and a modified nucleotide. *J Am Chem Soc* **2005,** *127* (30), 10510-1.

124. Li, Z.; Wu, J.; Deleo, C. J., RNA damage and surveillance under oxidative stress. *IUBMB Life* **2006,** *58* (10), 581-8.

125. Tretyakova, N. Y.; Groehler, A. t.; Ji, S., DNA-Protein Cross-Links: Formation, Structural Identities, and Biological Outcomes. *Acc Chem Res* **2015,** *48* (6), 1631-44.

126. U.S. Department of Health and Human Services , F. a. D. A., Center for Drug Evaluation and Research (CDER), Center for Biologics Evaluation and Research (CBER), Guidance for Industry, S2(R1) Genotoxicity Testing and Data Interpretation for Pharmaceuticals Intended for Human Use **2012**, 2.

127. Roos, W. P.; Kaina, B., DNA damage-induced cell death by apoptosis. *Trends Mol Med* **2006,** *12* (9), 440-50.

128. Loeb, K. R.; Loeb, L. A., Significance of multiple mutations in cancer. *Carcinogenesis* **2000,** *21* (3), 379-85.

129. Schins, R. P., Mechanisms of genotoxicity of particles and fibers. *Inhal Toxicol* **2002,** *14* (1), 57-78.

130. Chatterjee, N.; Walker, G. C., Mechanisms of DNA damage, repair, and mutagenesis. *Environ Mol Mutagen* **2017,** *58* (5), 235-263.

131. Minde, D. P.; Anvarian, Z.; Rudiger, S. G.; Maurice, M. M., Messing up disorder: how do missense mutations in the tumor suppressor protein APC lead to cancer? *Mol Cancer* **2011,** *10*, 101.

132. Taylor, S. I., Chapter 15 - Molecular Mechanisms in the Pathophysiology of Noninsulin-Dependent Diabetes Mellitus:: Insulin Resistance and Insulin Deficiency. In *Principles of Medical Biology*, Bittar, E. E.; Bittar, N., Eds. Elsevier: 1997; Vol. 10, pp 365-386.

133. Emerit, I., Reactive oxygen species, chromosome mutation, and cancer: possible role of clastogenic factors in carcinogenesis. *Free Radic Biol Med* **1994,** *16* (1), 99-109.

134. Xia, T.; Kovochich, M.; Liong, M.; Zink, J. I.; Nel, A. E., Cationic polystyrene nanosphere toxicity depends on cell-specific endocytic and mitochondrial injury pathways. *ACS Nano* **2008,** *2* (1), 85-96.

135. Hunter, A. C.; Moghimi, S. M., Cationic carriers of genetic material and cell death: a mitochondrial tale. *Biochim Biophys Acta* **2010,** *1797* (6-7), 1203-9.

136. Symonds, P.; Murray, J. C.; Hunter, A. C.; Debska, G.; Szewczyk, A.; Moghimi, S. M., Low and high molecular weight poly(L-lysine)s/poly(L-lysine)-DNA complexes initiate mitochondrial-mediated apoptosis differently. *FEBS Lett* **2005,** *579* (27), 6191-8.

137. Knop, K.; Hoogenboom, R.; Fischer, D.; Schubert, U. S., Poly(ethylene glycol) in drug delivery: pros and cons as well as potential alternatives. *Angew Chem Int Ed Engl* **2010,** *49* (36), 6288-308.

138. Luo, X.; Feng, M.; Pan, S.; Wen, Y.; Zhang, W.; Wu, C., Charge shielding effects on gene delivery of polyethylenimine/DNA complexes: PEGylation and phospholipid coating. *Journal of Materials Science: Materials in Medicine* **2012,** *23* (7), 1685-1695.

139. Li, S. D.; Huang, L., Stealth nanoparticles: high density but sheddable PEG is a key for tumor targeting. *J Control Release* **2010,** *145* (3), 178-81.

140. Diab KAE, E. A., Abd-Elmoneim OM, Sharaf HA, Assessment of Genotoxicity and Histopathological Changes Induced by Polyethylene Glycol (PEG6000) in Male Mice. *J Cytol Histol 3:153.* **2012**.

141. Dewachter, P.; Mouton-Faivre, C., Anaphylaxis to macrogol 4000 after a parenteral corticoid injection. *Allergy* **2005,** *60* (5), 705-6.

142. Armstrong, J. K.; Hempel, G.; Koling, S.; Chan, L. S.; Fisher, T.; Meiselman, H. J.; Garratty, G., Antibody against poly(ethylene glycol) adversely affects PEG-asparaginase therapy in acute lymphoblastic leukemia patients. *Cancer* **2007,** *110* (1), 103-11.

143. Richter, A. W.; Akerblom, E., Antibodies against polyethylene glycol produced in animals by immunization with monomethoxy polyethylene glycol modified proteins. *Int Arch Allergy Appl Immunol* **1983,** *70* (2), 124-31.

144. Imran ul-haq, M.; Lai, B. F.; Chapanian, R.; Kizhakkedathu, J. N., Influence of architecture of high molecular weight linear and branched polyglycerols on their biocompatibility and biodistribution. *Biomaterials* **2012,** *33* (35), 9135-47.

145. EFSA Panel on Food Contact Materials, E., Flavourings; (CEF), a. P. A., Scientific Opinion on the safety assessment of the substance, polyglycerol, CAS No 25618-55-7, for use in food contact materials. *EFSA Journal 2013;11(10):3389, 8 pp.* **2013**.

146. Gerecke, C.; Edlich, A.; Giulbudagian, M.; Schumacher, F.; Zhang, N.; Said, A.; Yealland, G.; Lohan, S. B.; Neumann, F.; Meinke, M. C.; Ma, N.; Calderon, M.; Hedtrich, S.; Schafer-Korting, M.; Kleuser, B., Biocompatibility and characterization of polyglycerol-based thermoresponsive nanogels designed as novel drug-delivery systems and their intracellular localization in keratinocytes. *Nanotoxicology* **2017,** *11* (2), 267-277.

147. Mugabe, C.; Liggins, R. T.; Guan, D.; Manisali, I.; Chafeeva, I.; Brooks, D. E.; Heller, M.; Jackson, J. K.; Burt, H. M., Development and in vitro characterization of paclitaxel and docetaxel loaded into hydrophobically derivatized hyperbranched polyglycerols. *Int J Pharm* **2011,** *404* (1-2), 238-49.

148. Du, F.; Honzke, S.; Neumann, F.; Keilitz, J.; Chen, W.; Ma, N.; Hedtrich, S.; Haag, R., Development of biodegradable hyperbranched core-multishell nanocarriers for efficient topical drug delivery. *J Control Release* **2016,** *242*, 42-49.

149. Honzke, S.; Gerecke, C.; Elpelt, A.; Zhang, N.; Unbehauen, M.; Kral, V.; Fleige, E.; Paulus, F.; Haag, R.; Schafer-Korting, M.; Kleuser, B.; Hedtrich, S., Tailored dendritic core-

multishell nanocarriers for efficient dermal drug delivery: A systematic top-down approach from synthesis to preclinical testing. *J Control Release* **2016,** *242*, 50-63.

150. Radbruch, M.; Pischon, H.; Ostrowski, A.; Volz, P.; Brodwolf, R.; Neumann, F.; Unbehauen, M.; Kleuser, B.; Haag, R.; Ma, N.; Alexiev, U.; Mundhenk, L.; Gruber, A. D., Dendritic Core-Multishell Nanocarriers in Murine Models of Healthy and Atopic Skin. *Nanoscale Res Lett* **2017,** *12* (1), 64.

151. Kainthan, R. K.; Gnanamani, M.; Ganguli, M.; Ghosh, T.; Brooks, D. E.; Maiti, S.; Kizhakkedathu, J. N., Blood compatibility of novel water soluble hyperbranched polyglycerol-based multivalent cationic polymers and their interaction with DNA. *Biomaterials* **2006,** *27* (31), 5377-90.

152. Zeng, H.; Schlesener, C.; Cromwell, O.; Hellmund, M.; Haag, R.; Guan, Z., Amino Acid-Functionalized Dendritic Polyglycerol for Safe and Effective siRNA Delivery. *Biomacromolecules* **2015,** *16* (12), 3869-77.

153. Ulbrich, K.; Etrych, T.; Chytil, P.; Jelinkova, M.; Rihova, B., Antibody-targeted polymer-doxorubicin conjugates with pH-controlled activation. *J Drug Target* **2004,** *12* (8), 477-89.

154. Alexiou, C., Nanomedicine - Basic and Clinical Applications in Diagnostics and Therapy. *Karger Medical and Scientific Publishers* **2011**, 160.

155. GM, C., The Cell: A Molecular Approach. 2nd edition. *Sunderland (MA): Sinauer Associates* **2000,** (Lysosomes).

156. Mastorakos, P.; Song, E.; Zhang, C.; Berry, S.; Park, H. W.; Kim, Y. E.; Park, J. S.; Lee, S.; Suk, J. S.; Hanes, J., Biodegradable DNA Nanoparticles that Provide Widespread Gene Delivery in the Brain. *Small* **2016,** *12* (5), 678-85.

157. Fischer, W.; Calderon, M.; Schulz, A.; Andreou, I.; Weber, M.; Haag, R., Dendritic polyglycerols with oligoamine shells show low toxicity and high siRNA transfection efficiency in vitro. *Bioconjug Chem* **2010,** *21* (10), 1744-52.

158. Fleige, E.; Quadir, M. A.; Haag, R., Stimuli-responsive polymeric nanocarriers for the controlled transport of active compounds: concepts and applications. *Adv Drug Deliv Rev* **2012,** *64* (9), 866-84.

159. Hellmund, M.; Achazi, K.; Neumann, F.; Thota, B. N.; Ma, N.; Haag, R., Systematic adjustment of charge densities and size of polyglycerol amines reduces cytotoxic effects and enhances cellular uptake. *Biomater Sci* **2015,** *3* (11), 1459-65.

160. Tschiche, A.; Thota, B. N.; Neumann, F.; Schafer, A.; Ma, N.; Haag, R., Crosslinked Redox-Responsive Micelles Based on Lipoic Acid-Derived Amphiphiles for Enhanced siRNA Delivery. *Macromol Biosci* **2016,** *16* (6), 811-23.

161. Dimde, M.; Steinhilber, D.; Neumann, F.; Li, Y.; Paulus, F.; Ma, N.; Haag, R., Synthesis of pH-Cleavable dPG-Amines for Gene Delivery Application. *Macromol Biosci* **2017,** *17* (1).

162. Dimde, M.; Neumann, F.; Reisbeck, F.; Ehrmann, S.; Cuellar-Camacho, J. L.; Steinhilber, D.; Ma, N.; Haag, R., Defined pH-sensitive nanogels as gene delivery platform for siRNA mediated in vitro gene silencing. *Biomater Sci* **2017,** *5* (11), 2328-2336.

7 Appendices

7.1 List of other Publications

(1) Chunhong Dong, Zhongyun Liu, Changzu Wu, **Falko Neumann**, Hanjie Wang, Monika Schäfer-Korting, Burkhard Kleuser, Jin Chang, Wenzhong Li, Nan Ma, Rainer Haag; *A Highly Photostable Hyperbranched Polyglycerol-Based NIR Fluorescence Nanoplatform for Mitochondria-Specific Cell Imaging*, Adv Healthc Mater. **2016** Sep;5(17):2214-26.

(2) Fang Du, Stefan Hönzke, **Falko Neumann**, Juliane Keilitz, Wei Chen, Nan Ma, Sarah Hedtrich, Rainer Haag; *Development of biodegradable hyperbranched core-multishell nanocarriers for efficient topical drug delivery*, J Control Release. **2016** Nov 28;242:42-49.

(3) Alexander Edlich, Christian Gerecke, Michael Giulbudagian, **Falko Neumann**, Sarah Hedtrich, Monika Schäfer-Korting, Marcelo Calderon, Burkhard Kleuser; *Specific uptake mechanisms of well-tolerated thermoresponsive polyglycerol-based nanogels in antigen-presenting cells of the skin*, Eur J Pharm Biopharm. **2017** Jul;116:155-163.

(4) Moritz Radbruch, Hannah Pischon, Anja Ostrowski, Pierre Volz, Robert Brodwolf, **Falko Neumann**, Michael Unbehauen, Burkhard Kleuser, Rainer Haag, Nan Ma, Ulrike Alexiev, Lars Mundhenk, Achim D Gruber; *Dendritic Core-Multishell Nanocarriers in Murine Models of Healthy and Atopic Skin*, Nanoscale Res Lett. **2017** Dec;12(1):64.

(5) Christian Gerecke, Alexander Edlich, Michael Giulbudagian, Fabian Schumacher, Nan Zhang, Andre Said, Guy Yealland, Silke B Lohan, **Falko Neumann**, Martina C Meinke, Nan Ma, Marcelo Calderon, Sarah Hedtrich, Monika Schäfer-Korting, Burkhard Kleuser; *Biocompatibility and characterization of polyglycerol-based thermoresponsive nanogels designed as novel drug-delivery systems and their intracellular localization in keratinocytes*, Nanotoxicology. **2017** Mar;11(2):267-277.

(6) Sabine Reimann, Tobias Schneider, Pia Welker, **Falko Neumann**, Kai Licha, Gundula Schulze-Tanzil, Wolfgang Wagermaier, Peter Fratzl and Rainer Haag; *Dendritic polyglycerol anions for the selective targeting of native and inflamed articular cartilage,* J. Mater. Chem. B **2017**, *5*, 4754-4767.

(7) Olaf Wagner, Bala N. S. Thota, Boris Schade, **Falko Neumann**, Jose L. Cuellar, Christoph Böttcher and Rainer Haag; *Perfluoroalkylated linear polyglycerols and their supramolecular assemblies in aqueous solution***,** Polym. Chem.**, 2016**,7, 2222-2229

(8) Stefano Stefani, Stefan Hönzke, Jose L C Camacho, **Falko Neumann**, Ashok K Prasad, Sarah Hedtrich, Rainer Haag, Paul Servin; *Hyperbranched glycerol-based core-amphiphilic branched shell nanotransporters for dermal drug delivery*. Polymer*,* **2016***,* 96, 156–166.

(9) Jianguang Zhang, Chen Wei, Leixiao Yu, Mingjun Li, **Falko Neumann**, Wenzhong Li, Rainer Haag, Nan Ma; *Selective Endothelial Cell Adhesion Via Mussel-Inspired Hybrid Microfibrous Scaffold.* ACS Appl. Mater. Interfaces, **2018**, submitted

(10) Era Kapourani, **Falko Neumann**, Katharina Achazi, Jens Dernedde and Rainer Haag; *Droplet-Based Microfluidic Templating of Polyglycerol-Based Multifunctional Microgels for the Encapsulation of Cells. A Comparative Study***.** J. Mater. Chem. B**, 2018**, submitted

7.2 Abbreviations

4-HNE *4-hydroxynonenal*

ADME ..... *Absorption, Distribution, Metabolism, Excretion*

bPEI ..... *branched polythyleneimine*

CME ..... *Clathrin mediated endocytosis*

CvME ..... *Caveolin-mediated endocytosis*

DDS ..... *Drug Delivery System*

dPG ..... *dendritic polyglycerol*

EFSA ..... *European Food Safety Authority*

FLIM ..... *Fluorescence Lifetime Imaging Microscopy*

GSH ..... *Glutathione*

HPG ..... *hyperbranched polyglycerol*

LPG ..... *linear polyglycerol*

miRNA ..... *micro RNA*

MPS ..... *mononuclear phagocyte system*

NA ..... *Nucleic Acid*

NADPH ..... *Nicotinamide adenine dinucleotide phosphate*

NP ..... *Nanoparticle*

PBAE ..... *poly(ß-amino ester)*

PEG ..... *Polyethleneglycol*

PEI ..... *Polyethyleneimine*

PG ..... *Polyglycerol*

PM_{10} ..... *particulate matter with a size below 10 µm*

$PM_{2.5}$.....*particulate matter with a size below 2.5 µm*
RES .....*Reticuloendothelial system*
RISC .....*RNA-Induced Silencing Complex*
RNS..... *Reactive nitrogen species*
ROS..... *Reactive oxygen species*
siRNA.....*small interfering RNA*
SOD .....*Superoxide dismutase*